

COMPONENTS' AND MATERIALS' PERFORMANCE FOR ADVANCED SOLAR SUPERCRITICAL CO2 POWERPLANTS

Report on manufactured particles/sCO2 heat exchanger

Deliverable Number 5.3

WP5 Technology validation

Date: 15 April 2025

Deliverable type: Report

Dissemination level: Public

Lead participant: CVR





This project has received funding from the European Union's Horizon 2020 Research and Innovation Action (RIA) under grant agreement No. **958418.**

AUTHORS

Name	Organization
Radomir Filip	CVR
Miroslav Říha	CVR
Otakar Frýbort	CVR

DOCUMENT HISTORY

Version	Date	Change
01	15/04/2025	Initial version uploaded

ABOUT THE PROJECT

COMPASsCO₂ is a 4,5-year HORIZON2020 project started on 1.11.2020. It is led by the German Aerospace Center (DLR), with eleven additional partners from seven European countries.

COMPASsCO₂ aims to integrate CSP particle systems into highly efficient s-CO₂ Brayton power cycles for electricity production. In COMPASsCO₂, the key component for such an integration, i.e. the particle/s-CO₂ heat exchanger, will be validated in a relevant environment. To reach this goal, the consortium produced tailored particle and alloy combinations that meet the extreme operating conditions in terms of temperature, pressure, abrasion and hot oxidation/carburization of the heat exchanger tubes and the particles moving around/across them. The proposed innovative CSP s-CO₂ Brayton cycle plants will be flexible, highly efficient, economic and 100% carbon neutral large-scale electricity producers.

The research focus of COMPASsCO2 is on three main technological improvements: development of new particles, development of new metal alloys and development of the heat exchanger section.

DISCLAIMER

This project has received funding from the European Union's Horizon 2020 Research and Innovation Action (RIA) under grant agreement No. **958418.**

The content of this publication reflects only the author's view and not necessary those of the European Commission. The Commission is not responsible for any use that may be made of the information this publication contains.

1

TABLE OF CONTENTS

Lis	t of I	Figures	. 3
Lis	t of ⁻	Tables	. 4
Lis	t of	Abbreviations	. 5
1	Inti	roduction	. 6
2	ope	eration conditions	. 6
3	Ма	nterials selection	. 6
4	De	sign & Specifications	. 7
5	Sa	fety features	. 8
6	Ins	strumentation & equipment	10
7	Str	ess analysis	11
8	Pe	rformance estimation	13
8	3.1	heat insulation and Heat loss estimation	13
8	3.2	Thermal performance	14
9	CC	DNCLUSIONS	16
10	F	Annexes	19
1	0.1	Annex 1. Declaration of conformity	19
1	0.2	Annex 2. Heat exchanger – technical drawings	21
-	0.3	Annex 3. Particle Cold test experiments overview	23

LIST OF FIGURES

Figure 1: HX cross-section - Tube arrangement	8
Figure 2: CAD model of the heat exchanger - isometric view	9
Figure 3: Heat exchanger with the installed safety features	10
Figure 4: Heat exchanger temperature probes placement	11
Figure 5: Temperature field of the modelled section	12
Figure 6: von-Mises stress [MPa], operational regime	13
Figure 7: The schematics of the resulted temperature profile over the insulation	layer.
Figure 8: The shape of the particle's stagnation/void zone along the	tube's
circumference	
Figure 9: Heat exchanger during the fabrication - near completion	
Figure 10: Fully assembled heat exchanger	
Figure 11: Scheme of the particles cold test experimental rig	
Figure 12: Fabricated cold test experimental rig	
Figure 13: Multicolour particle mixture SB 30/50.	
Figure 14: Tube configuration layout.	
Figure 15: Screw for conveying the particles	
Figure 16: Particles mass-flow characteristics of the screw conveyor	
Figure 17: Pressure loss per 1m in vertical pipe during the particle transportation	
Figure 18: Configuration 1 - velocity field - MPF = 168g/s	
Figure 19: Configuration 3 - velocity field - MPF = 168g/s	
Figure 20: Configuration 3 - velocity field - MPF = 67g/s	
Figure 21: Measuring the height and angle section of the stagnation zones	
Figure 22: The function of the top stagnation zone height	
Figure 23:The function of the bottom stagnation zone height	
Figure 24: Angle displacement scheme	
Figure 25: Angle displacement sensitivity - radial distribution	
Figure 26: Model of the stagnation zones around a single tube D=19.05; VP/D	
Figure 27: Plotted individual heat transfer resistances for a single tube D=19.05;	
= 1.5	
Figure 28: Comparison of the total heat transfer resistance for various VP/D rati	os. 42

LIST OF TABLES

Table 1: Operating conditions of the heat exchanger	6
Table 2: Material properties Inconel 625 for selected temperatures	7
Table 3: Material properties AISI 316Ti for selected temperatures	7
Table 4: Thermal conductivity (W/mK) of chosen thermal insulation materials	at various
temperatures	13
Table 5: Estimated thermal performance of the heat exchanger	15
Table 6: Overview of the tube configuration parameters	27
Table 7: Measured data from the particle velocity fields	33
Table 8: List of considered variables.	39
Table 9: Comparison of average heat transfer resistances for different ve	rtical tube
spacing	42

LIST OF ABBREVIATIONS

COMPASsCO2 Components' and Materials' Performance for Advanced Solar

Supercritical CO2 Power Plants

CST Concentrating Solar Thermal

CVR Research Centre Řež s.r.o.

DLR German Aerospace Centre

EC European Commission

EU European Union

IN Inconel

JCR John Cockerill Renewables

LMTD Logarithmic mean temperature difference

HX Heat exchanger

sCO₂ Supercritical carbon dioxide

1 INTRODUCTION

The objective of this document is to present key aspects of the design and manufacturing of the particles/sCO₂ heat exchanger mockup. This prototype was developed, manufactured, and tested at CVR with significant support of JCR and DLR during the design phase. The primary purpose of these tests is to demonstrate the operation of a system where two novel technologies at extreme operation conditions are integrated, providing valuable data on thermal performance and model validation.

2 OPERATION CONDITIONS

The working pressure of the HX is 25 MPa, while the design pressure is set to 26.5 MPa. As described in the next chapter, due to the used materials and safety reasons, the operating pressure on the sCO_2 side was limited to 15 MPa. However, this limitation will not negatively impact the quality of the test data, as the thermophysical properties of carbon dioxide such as thermal conductivity, heat capacity and viscosity are not highly dependent on pressure. Table 1. provides an overview of the design pressures and temperatures. Note that the tube's outer wall will be exposed to particle bulk temperatures of up to 850°C. Due to significantly higher heat transfer coefficient at sCO_2 side, the outer wall temperature is expected to remain below 745°C, as estimated from thermal analysis. The resulted temperature field is shown in Figure 5.

	sCO2 side	Particles side
Design Inlet temperature (°C)	535	850
Design Outlet temperature (°C)	700	730
Design pressure (MPa)	26.5	0.04
Operating pressure (MPa)	15	-

Table 1: Operating conditions of the heat exchanger.

3 MATERIALS SELECTION

Originally, the heat exchanger was intended to be fabricated from Haynes 282, as it met the required strength criteria for the initial operating conditions (25 MPa). However, due to budget constraints and long delivery time, sourcing this material was beyond the project's scope. The second material choice was IN740H, but after many difficulties with the material supplier this option had to be declined and finally Inconel 625 was selected due to availability in the market. Inconel 625 was therefore used for the tube banks containing high-pressure CO₂, while AISI 316Ti

was used for the casing that holds the particles. These materials allow to demonstrate the HX performance within a limited lifetime of a few days but are not suitable for long-term operation of an industrial application. Tables detailing the material properties are provided below.

Inconel 625	600°C	700°C	760°C
Young modulus (GPa)	171	163	157
Poisson number (-)	0.31	0.31	0.31
Yield strength (MPa)	398	387	381
Tensile strength (MPa)	825	725	609
Thermal expansion coefficient (K ⁻¹)	1.44E-5	1.50E-5	1.53E-5

Table 2: Material properties Inconel 625 for selected temperatures.

Table 3: Material properties AISI 316Ti for selected temperatures.

AISI 316Ti	600°C	700°C	800°C	900°C
Young modulus (GPa)	155	146	138	131
Poisson number (-)	0.3	0.3	0.3	0.3
Yield strength (MPa)	121	113	105	96
Tensile strength (MPa)	310	260	210	160
Thermal expansion coefficient (K ⁻¹)	1.85E-5	1.90E-5	1.95E-5	2.00E-5

4 DESIGN & SPECIFICATIONS

The heat exchanger is designed as shell-and-tube type, with high pressure CO₂ contained within tubes of diameter 21.3 mm and wall thickness 2.77 mm. The tubes are arranged in two passes per stage with a horizontal pitch of 30.3 mm, resulting in a 9 mm gap between tubes, which is roughly 10 times the particle diameter and lays within the recommended range for optimal particle flow and thus maximum heat transfer from the particles to the CO₂.

The heat exchanger consists of 26 stages with a vertical pitch of 66.5 mm, selected to accommodate the manufacturability of the bends connecting the stages. Additionally, the vertical pitch-to-tube diameter ratio exceeds 3, which falls within the optimal range, where the particles stagnation layer on top of the tube is minimized, thereby reducing thermal resistance. These findings are based on cold flow experiments and are thoroughly documented in the Annex 3. Particle Cold test experiments overview.

The tube banks are submerged in the moving bed of particles, contained within the casing, which forms a channel for the particles, measuring 85 mm in width, 490 mm in length and roughly 1711 mm in height. To ensure optimal particle flow distribution around the tube banks, the casing is equipped with "tube half-wall" flow restrictors. Figure 1 illustrates the heat exchanger's tube banks layout and dimensions in the cross-section.

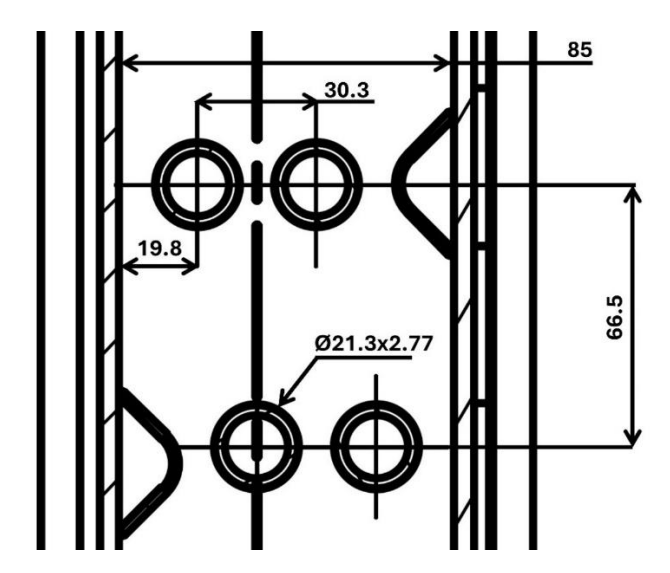


Figure 1: HX cross-section - Tube arrangement

5 **SAFETY FEATURES**

The heat exchanger is equipped with multiple layers safety features to mitigate potential risks and ensure safe operation.

The **primary protection layer** is an active system designed to address scenarios involving a loss of sCO_2 mass flow. In such cases, the tubes may overheat due to the absence of internal cooling, potentially leading to rupture. To prevent this, the control system automatically responds by opening valves to rapidly depressurize the sCO_2 within the tube bank. Simultaneously, the operator can manually activate the emergency release valve on the particle side (shown in Figure 3), allowing the particles to be discharged into a catch tank, thereby preventing further overheating.

The **secondary protection layer** is a passive system designed to manage tube rupture scenarios. A sudden tube failure would cause a rapid pressure increase within the particle bed. To counter this, shareable fasteners secure blast covers, as shown in Figure 2. In the event of a rupture, these fasteners break, directing the blast through

the front side of the heat exchanger, where it is contained within a blast shield, as illustrated in Figure 3.

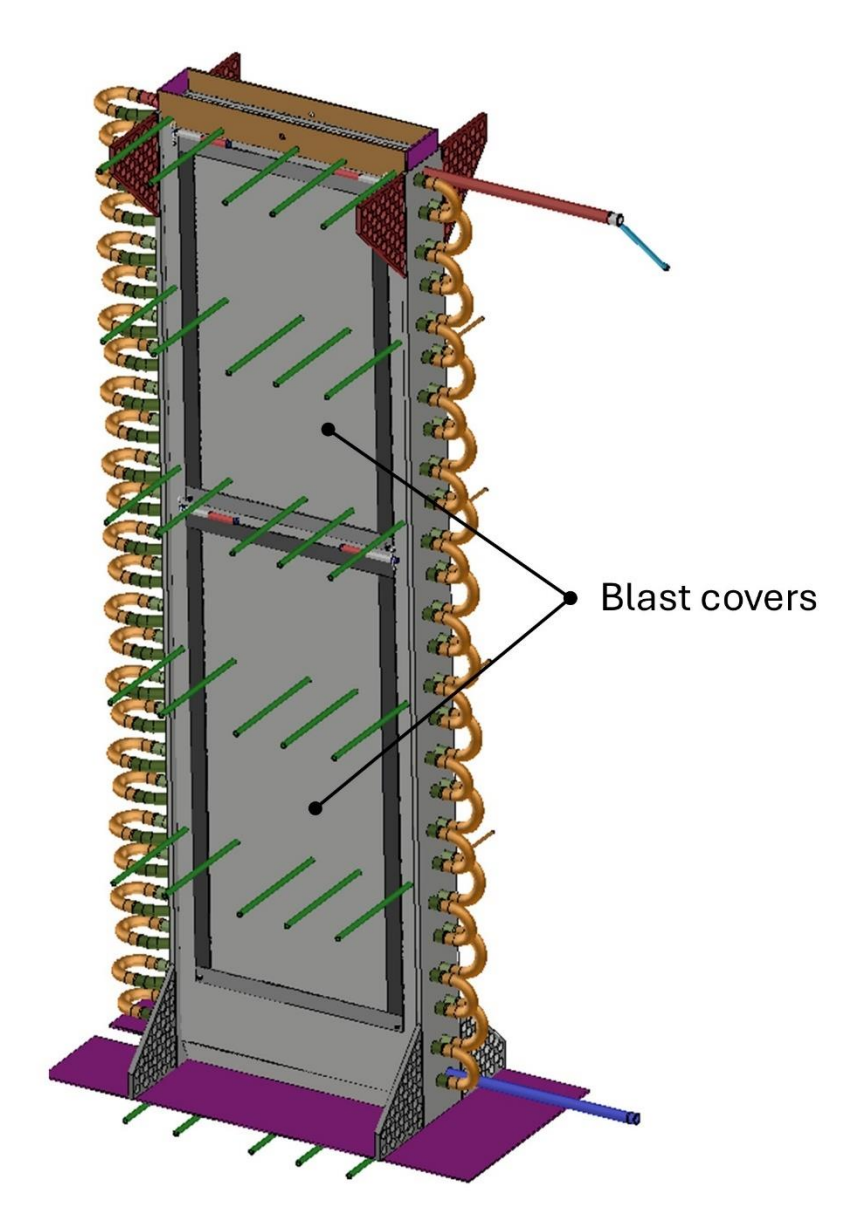


Figure 2: CAD model of the heat exchanger - isometric view.

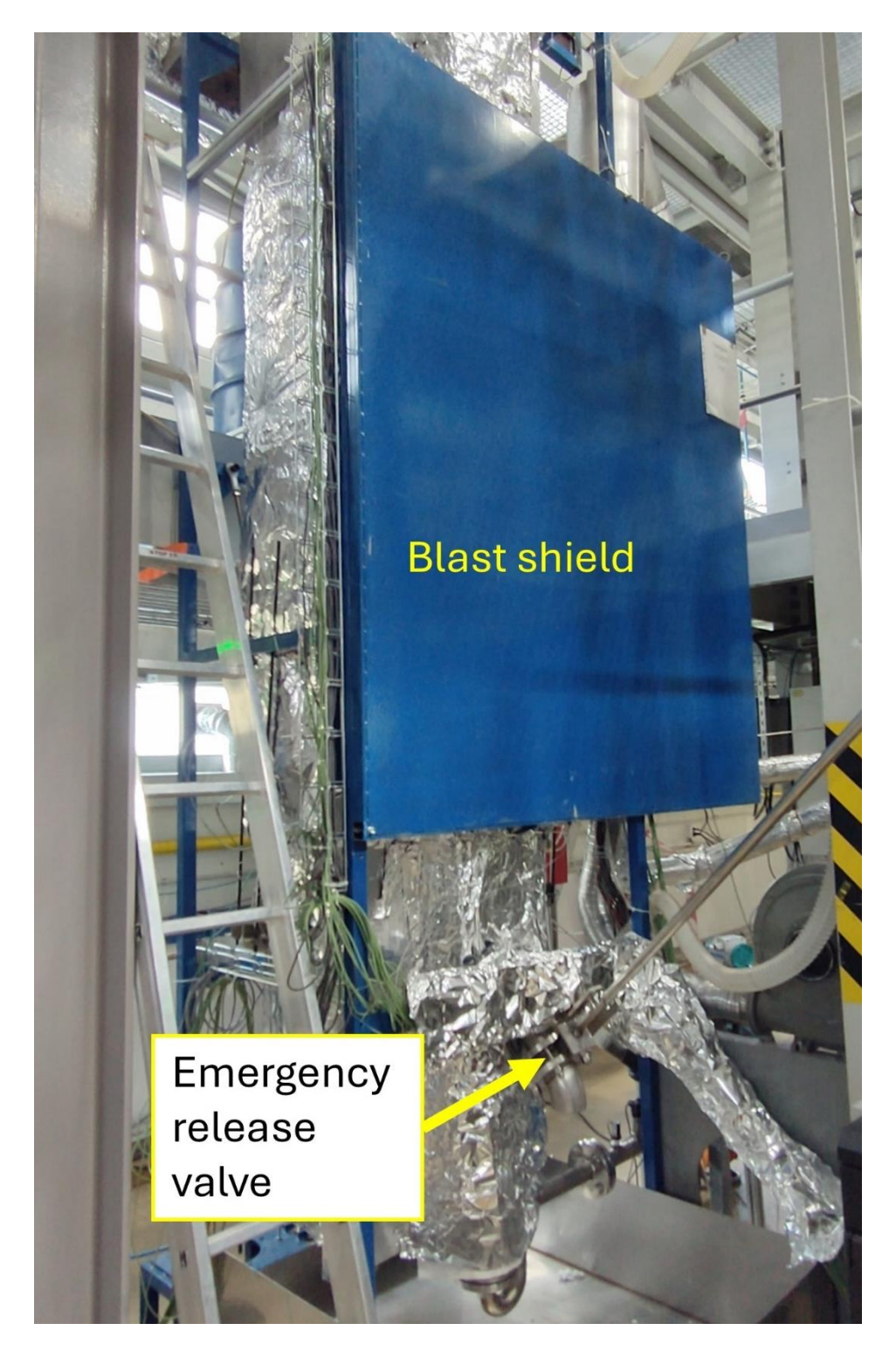


Figure 3: Heat exchanger with the installed safety features.

6 INSTRUMENTATION & EQUIPMENT

The heat exchanger is equipped with multiple temperature measurement probes for accurate thermal monitoring. A total of 20 Type K thermocouples are embedded within ceramic sumps that are in direct contact with the particles. These sumps are positioned at four height levels, with each row containing five evenly spaced probes,

allowing for a detailed temperature profile within the heat exchanger. The placement of these probes is illustrated in Figure 4.

Additionally, on the sCO_2 side, indirect thermocouples are attached to the outer wall of the tube banks at corresponding positions, as shown in Figure 4. At the heat exchanger inlet, direct temperature measurement is provided by three PT100 probes, followed by three indirect temperature measurements using thermocouples attached to the outer wall. This setup allows for the evaluation of deviations between direct and indirect measurement methods, as direct measurement at the sCO_2 outlet was not feasible due to high temperatures. As a result, the sCO_2 outlet temperature will be measured only indirectly.

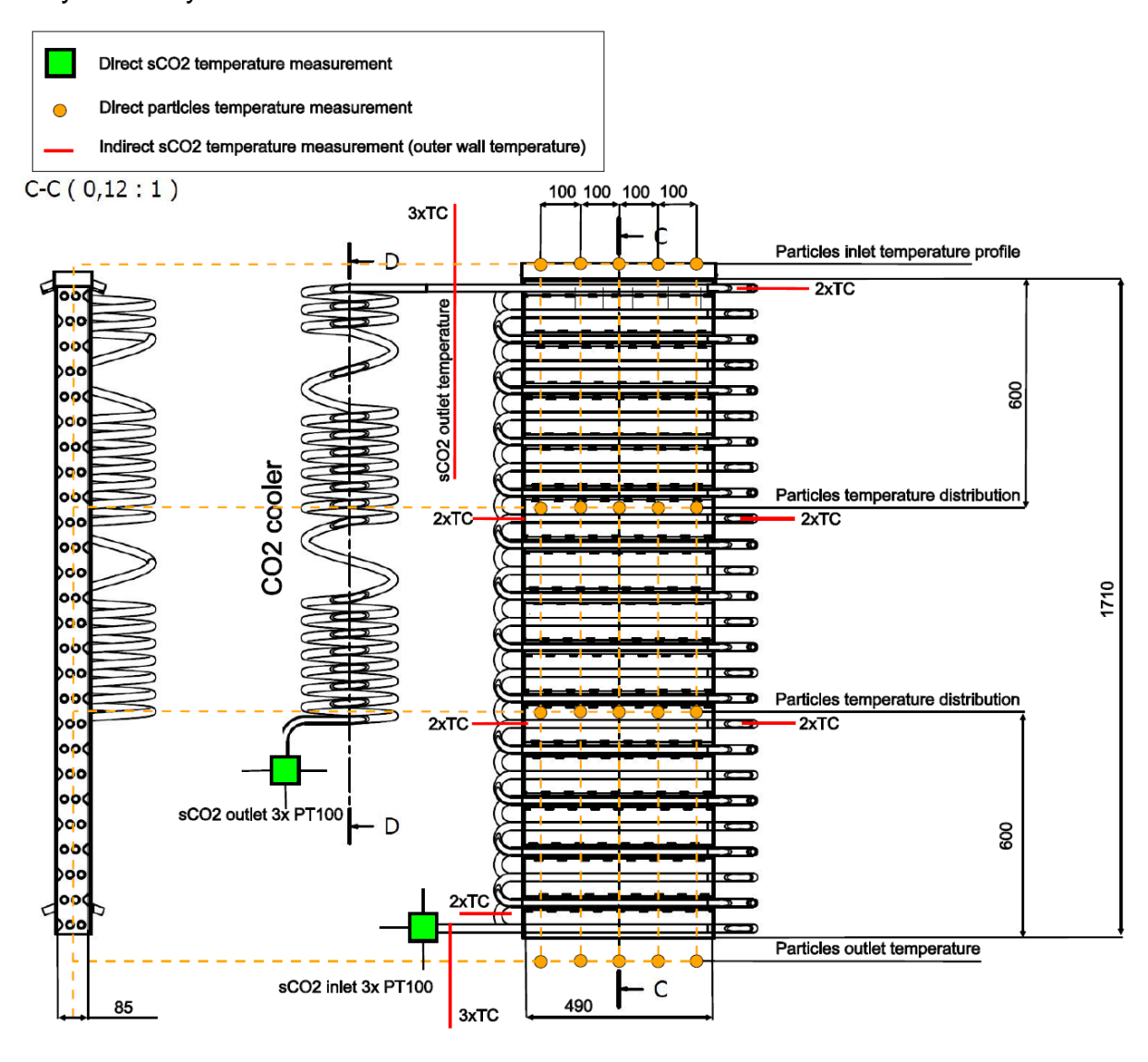


Figure 4: Heat exchanger temperature probes placement.

7 STRESS ANALYSIS

Static strength calculations were conducted using finite element method (FEM). Two load cases were analysed: the operational regime and the pressure test. Only the most stressed region, namely the inlet area, where the temperature is highest, was

considered. If the most stressed part of the component passes, the rest can be assumed to pass as well. The model included both the piping and the side walls of the casing and considered their interaction under elevated temperature. Due to the different coefficients of thermal expansion of the two used materials, frictionless contacts were used to allow axial movement of the pipes through the casing while maintaining contact. In the operational regime analysis, the model was subjected to an internal pressure of 26.5 MPa and a temperature field derived from CFD analysis, as illustrated in Figure 5. The pressure test was modelled in accordance with EN 13445, the temperature effects were neglected, and the internal pressure increased to 73.42 MPa. The Figure 6 shows the resulting von-Misses stress distribution of operational regime.

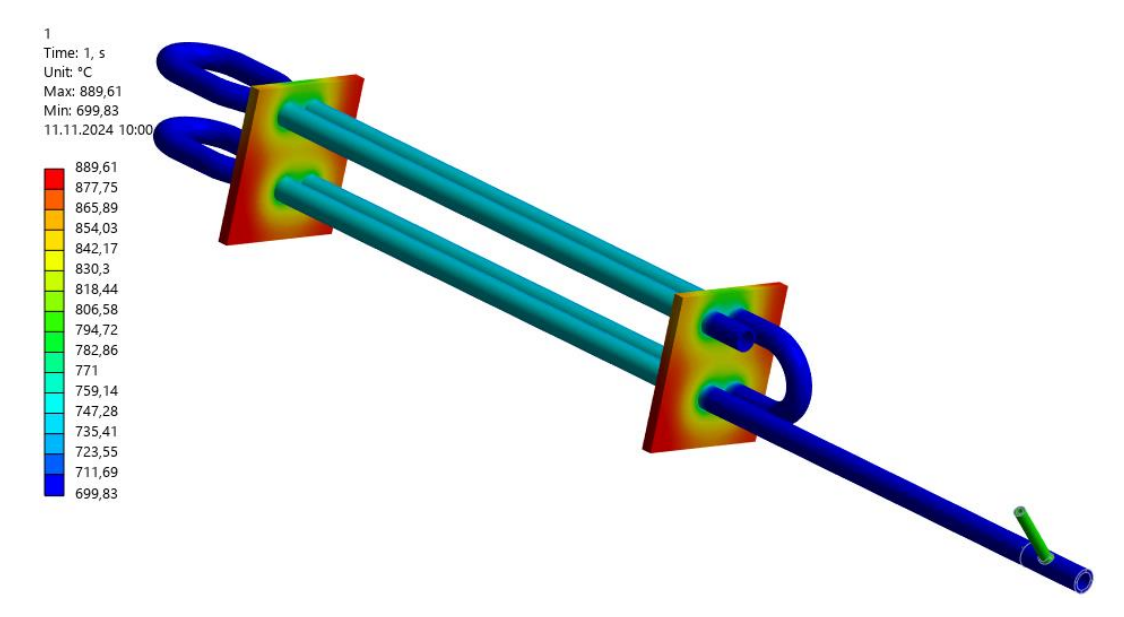


Figure 5: Temperature field of the modelled section.

The evaluation was carried out using the critical section method in accordance with CSN EN 13445. Several sections were extracted from the model, along which the calculated stresses were linearized and categorized into membrane and bending components. The values of allowable stresses specified by the standard were based on the yield strength and tensile strength at the given temperature. Their values were 215.9 MPa for the operational regime and 478.5 MPa for the pressure test. A welded joint coefficient of 0.85 was applied in the allowable stress calculations for the operational regime. The calculated stresses in all critical sections remained within the allowable limits, confirming that the heat exchanger meets the static strength requirements for both the operational regime and the pressure test.

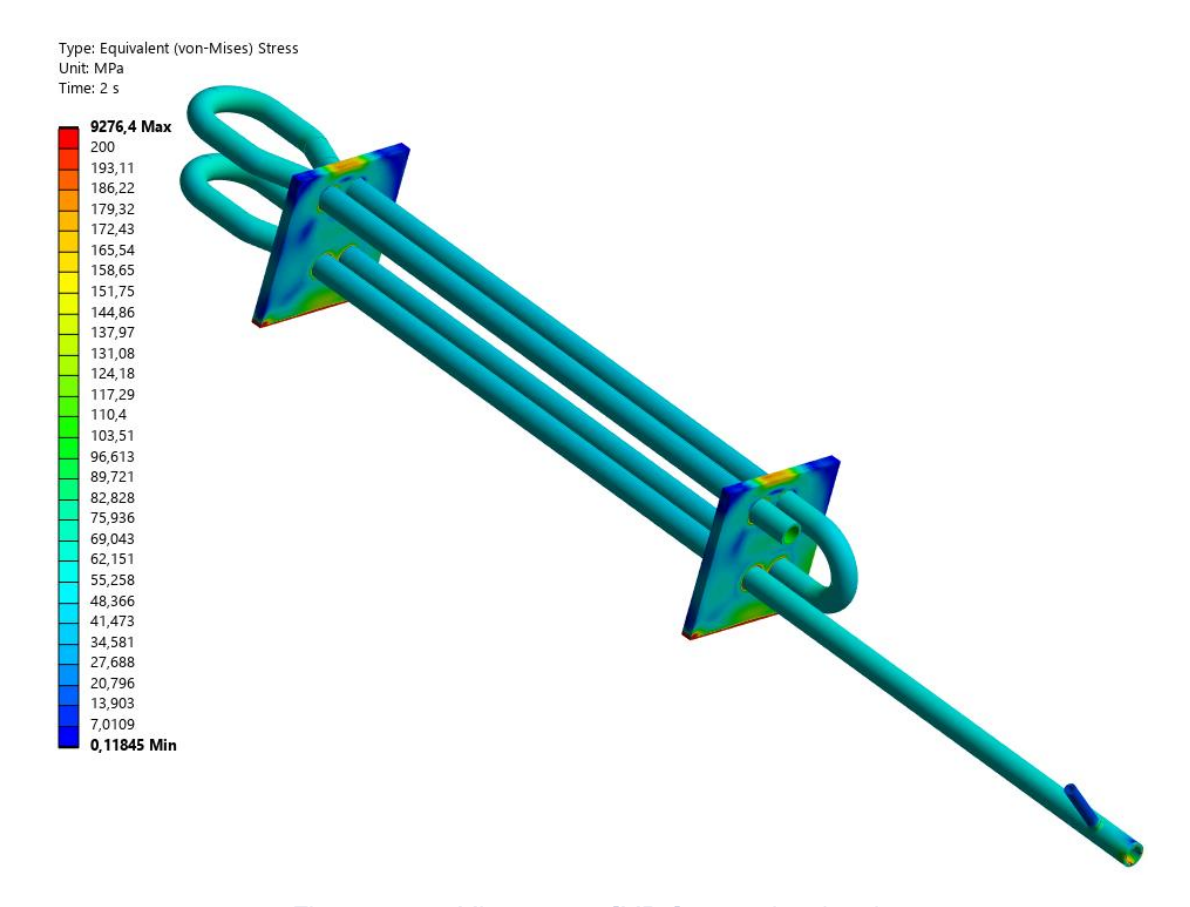


Figure 6: von-Mises stress [MPa], operational regime

8 PERFORMANCE ESTIMATION

8.1 HEAT INSULATION AND HEAT LOSS ESTIMATION

A simple thermal conduction model was used to estimate the heat losses based on the selected thermal insulation materials. Two types of insulation were chosen: mineral wool (Fiberfrax), which is in direct contact with the heat exchanger casing, and microporous blocks (WDS Ultra), which form the outer enclosure. The thermal conductivity of these materials at various temperatures is listed in table below.

Table 4: Thermal conductivity (W/mK) of chosen thermal insulation materials at various temperatures.

	Fiberfrax	WDS ultra
200°C	0.07	0.02
400°C	0.11	0.024
600°C	0.12	0.031
800°C	0.18	0.04

The geometry used for the heat loss estimation is based on the heat exchanger dimensions and was simplified as a block, with the surface area increasing as additional insulation thickness are applied. The results indicate that a 100mm thick layer of mineral wool, combined with an additional 50mm layer of microporous insulation, should be sufficient to maintain the outer wall temperature bellow 65°C, with an estimated heat loss of around 1100W. The schematics of the resulted temperature profile over the insulation layers is illustrated in Figure 8.

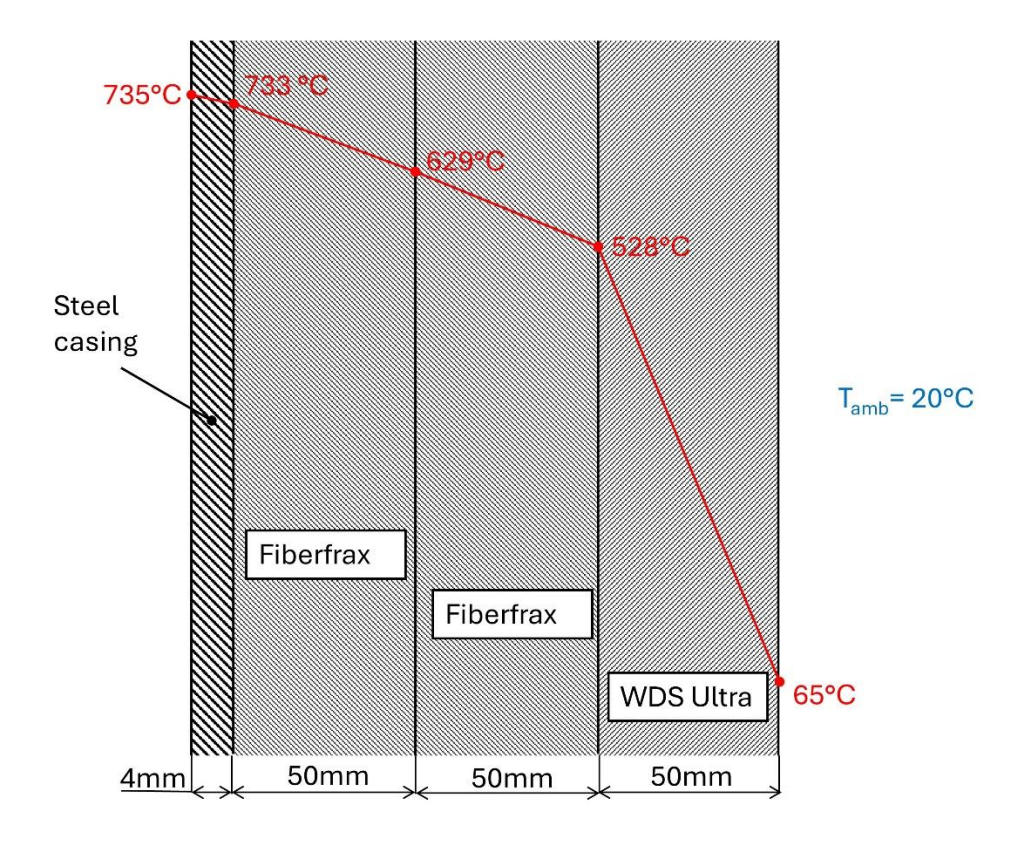


Figure 7: The schematics of the resulted temperature profile over the insulation layer.

8.2 THERMAL PERFORMANCE

The thermal performance was estimated based on the findings from cold flow experiments, where the shape and size of the particle's stagnation zone was observed. It was theorized that this stagnation zone directly influences thermal resistance, which varies along the tube's circumference. The methodology for determining thermal resistance is described in the Annex 3. Particle Cold test experiments overview.

These findings were applied to the current heat exchanger geometry, and the resulting shape of the stagnation zone was modelled as shown in Figure 8. The resulting parameters of the heat exchanger are shown in Table 5, where the heat loss was assumed to be twice the initially estimated value.

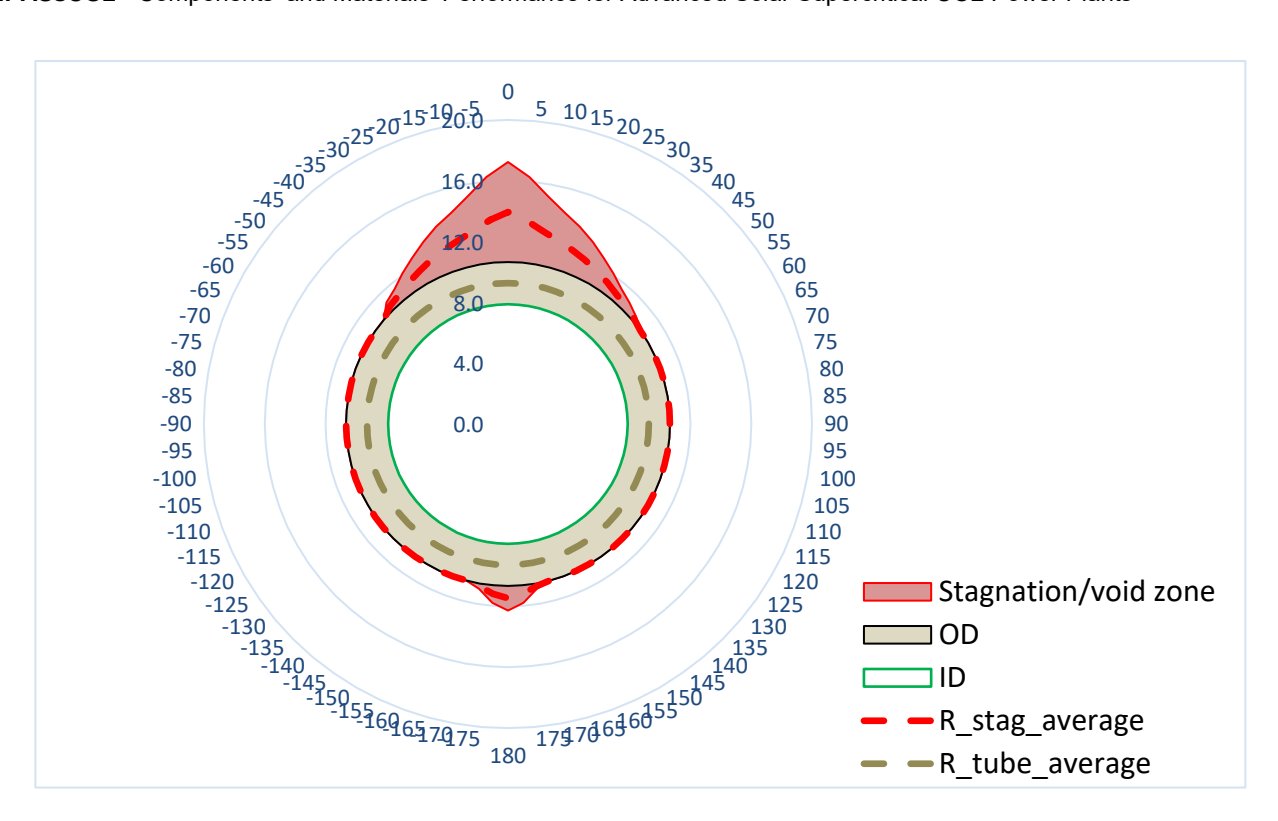


Figure 8: The shape of the particle's stagnation/void zone along the tube's circumference.

Table 5: Estimated thermal performance of the heat exchanger.

Average thermal resistance (mK/W)	0.147
Effective tube length (m)	25.48
Particles outlet temperature (°C)	723
LMTD (°C)	168.1
Heat loss (W)	2200
Heat transferred (W)	25476

9 **CONCLUSIONS**

The fabrication of the heat exchanger was carried out in CVR's workshop. All tube weld joints were inspected using dye penetrant and radiographic testing methods. To ensure structural integrity, a hydrostatic pressure test was performed at 432 bar.

The entire fabrication and testing process complied with the relevant regulations and standards, as documented in the Declaration of Conformity provided in Annex 1. A snapshot of the fabrication process is shown in Figure 9, while Figure 10 depicts the completed heat exchanger fully assembled in the test frame. Furthermore, the technical drawing of the main assembly is contained within Annex 2.

Detailed test results and data will be presented in Deliverable 5.4.



Figure 9: Heat exchanger during the fabrication - near completion.



Figure 10: Fully assembled heat exchanger.

10 ANNEXES

10.1 ANNEX 1. DECLARATION OF CONFORMITY



Centrum výzkumu Řež s.r.o. Hlavní 130 Husinec-Řež 250 68 E-mail: <u>cvrez@cvrez.cz</u> tel.: +420 266 173 181 IČ: 26722445

Under Directive 2014/68/EU of the European Parliament and of the Council, transposed Act No. 90/2016 Coll., as amended, and Government Regulation No. 219/2016 Coll., as amended We publish

EU DECLARATION OF CONFORMITY

product - pressure equipment

Name: ASSEMBLY HX_COOLER

Project: COMPASS

Type: Pressure vessel - pipe

Serial number: Compass/25_1 (COMP-034-25)

Compass/25_2 (COMP-340-24)

Year od production: 2025
Category / module acc. to PED: -/-

Description: A device for measuring heat transfer between solid particles and

supercritical CO2.

Producer: Centrum výzkumu Řež s.r.o.

Husinec-Řež č.p. 130, 250 68 Husinec-Řež

Company ID: 26722445

List of regulations used:

- Directive of the European Parliament and of the Council 2014/68/EU
- Law no. 90/2016 Sb., as amended
- Government Decree no. 219/2016 Sb., as amended
- Technical standards: EN 13445, EN 13480, ČSN EN ISO 9712, ČSN EN 10204, ČSN EN ISO 15614 -1, ČSN EN 9606, ČSN EN ISO 5817, ČSN EN ISO 23277, ČSN EN 12517-1

Entity that has assessed the quality system:

Business name: DNV GL – Business Assurance Situated: Thákurova 4, 160 00 Praha

strana 1 z 2



Centrum výzkumu Řež s.r.o. Hlavní 130 Husinec-Řež 250 68

250 68
E-mail: <u>cvrez@cvrez.cz</u>
tel.: +420 266 173 181
IČ: 26722445

The following documents were used for the conformity assessment:

- Quality Management System Certificate ISO 9001:2015 no. 207944-2016-AQ-CZS-RvA of the day 15.10.2022
- Certificate of compliance with quality requirements for arc welding of metallic materials ISO 3834-2:2021 no. 268283-2018-AQ-CZS-FINAS of the day 07.09.2024
- Environmental management system certificate ISO 14001:2015 no. 207945-2016-AE-CZS-RvA of the day 15.10.2022
- Safety Management System Certificate ISO 45001:2018 no. 207946-2016-AHSO-CZS-RvA of the day 15.10.2022

We confirm on our own responsibility that the properties of the product specified in this declaration meet the requirements of Directive 2014/68/EU of the European Parliament and of the Council, implemented by Act No. 90/2016 Coll., as amended, and Government Regulation No. 219/2016 Coll., as amended, that the product is safe under normal use, i.e. specified in the Instructions for Use.

YOCIC,

Location:

Signature:

Date:

Executive CVŘ:

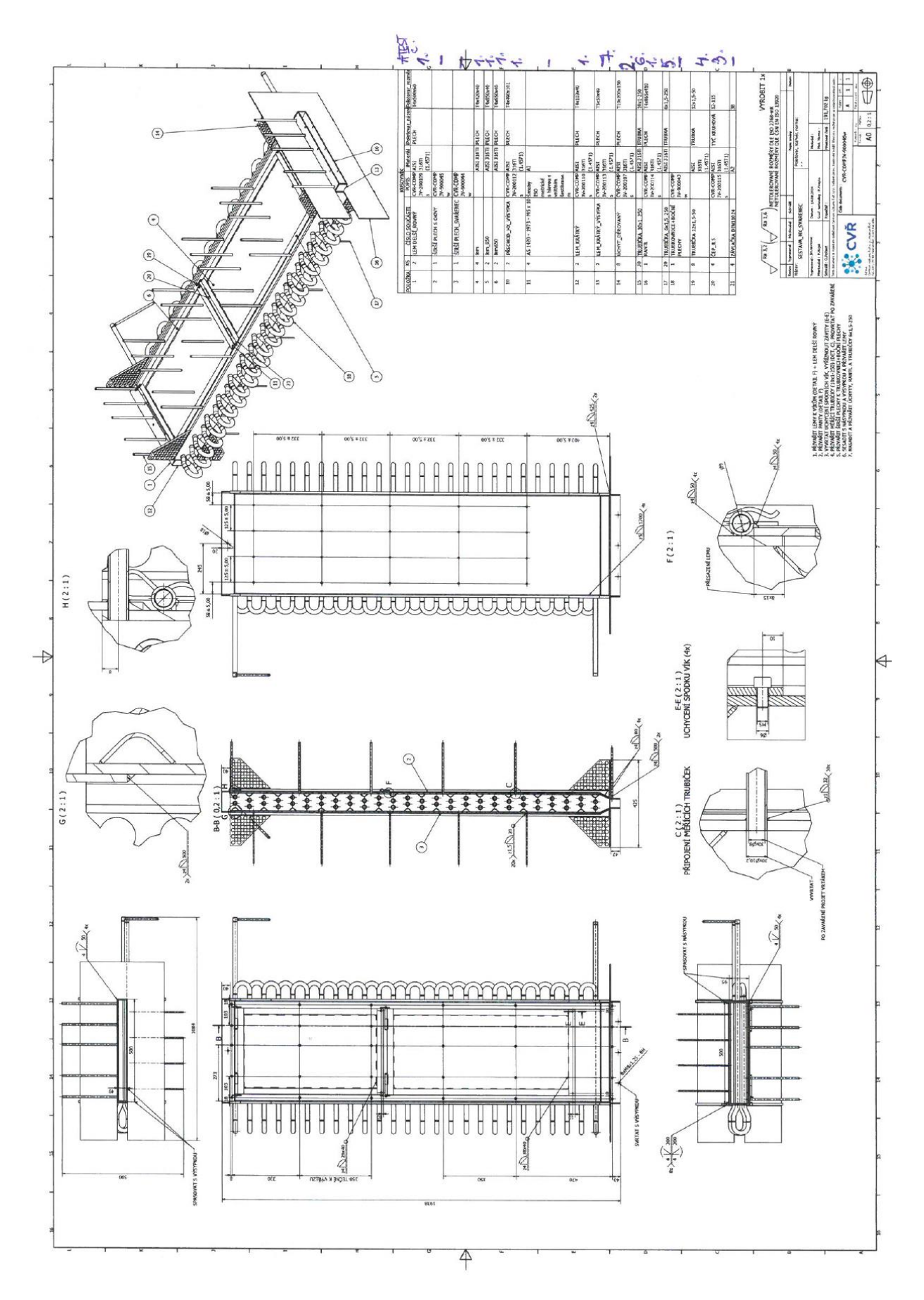
Executive CVŘ: Signature:

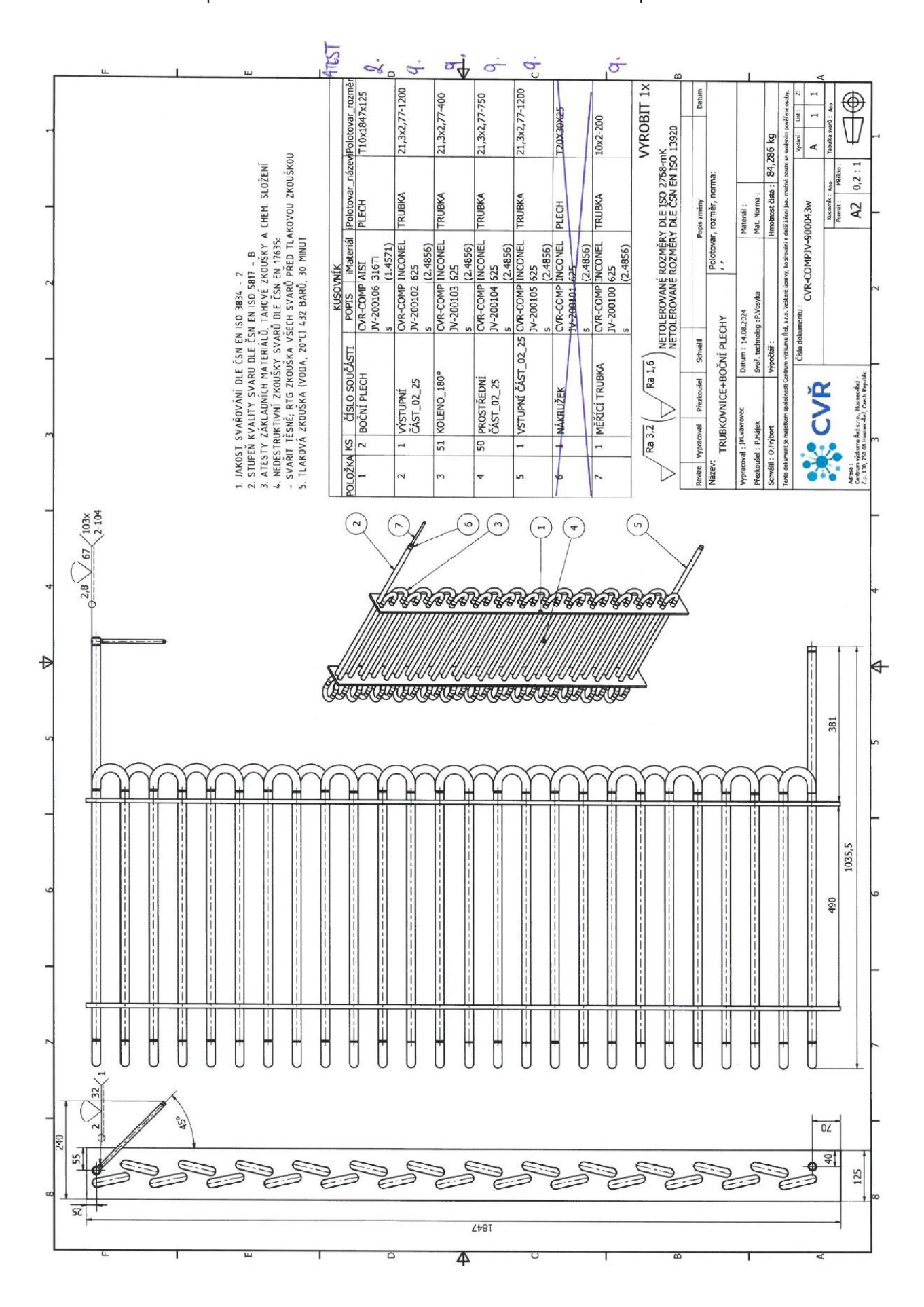
Husinec-Řež 11.3.2025

Ing. Milan Patrík, MBA

Ing. Petr Březina

10.2 ANNEX 2. HEAT EXCHANGER - TECHNICAL DRAWINGS





10.3 ANNEX 3. PARTICLE COLD TEST EXPERIMENTS OVERVIEW

Description

The purpose of the cold test experiments is to examine the particle flow field between the tube banks, that represent the particles heat exchanger, for various tube configurations and flow regimes at ambient temperatures. Furthermore, the characteristics of the proposed particle transportation system were tested. For this reason, an experimental rig was fabricated, schematically shown in Figure 11. It consists of open loop air transportation system, where the air, which is propelled with blower, is carrying the tested particles, that are delivered into the air flow with a screw conveyor. The particles are separated from the air in the cyclone separator and fed in to the hopper. The air is further filtered and outflows into the ambient. The hopper is divided from the test section by a door hatch. The test section is made of transparent plexi-glass sheets, which allow to directly observe the particle flow. The plexi-glass sheets contain pre-cut holes with certain tube configuration which are interchangeable. The distance between two plexi-glass sheets that is considered as a channel depth is 80mm. The channel width can slightly vary according to the used tube configuration in range of <230; 280> mm. The particle mass flow can be adjusted by varying the revolutions of the screw conveyor. The experimental rig is also equipped with instrumentation allowing to monitor the air flow and pressure difference. Fabricated experimental rig is shown in Figure 12.

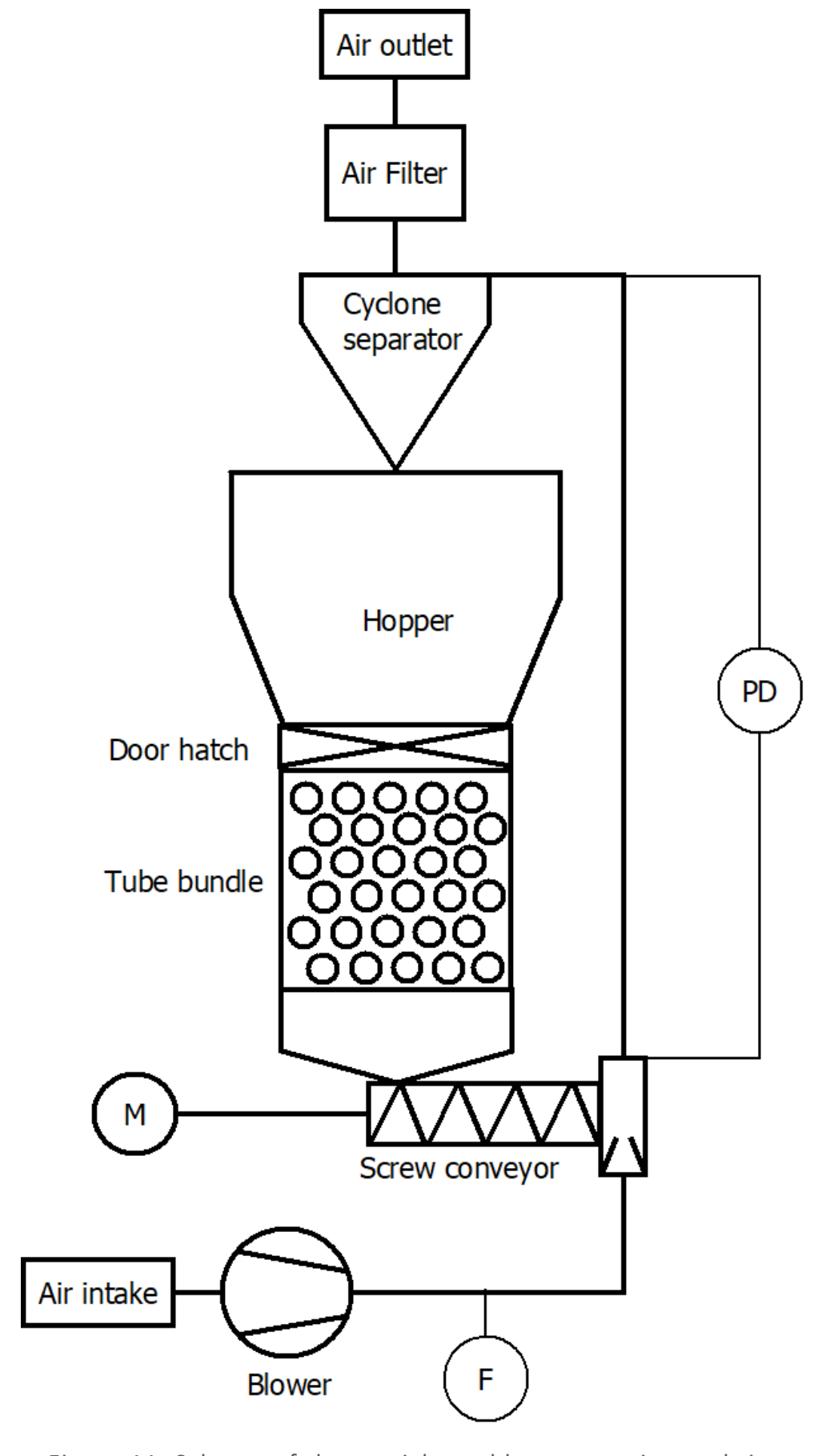


Figure 11: Scheme of the particles cold test experimental rig.



Figure 12: Fabricated cold test experimental rig.

Tested particles

All the tests were performed with the Sintered Bauxite 30/50 particles, where the spherical grains are ranging in size from 0.3 - 0.6 mm. To obtain some optical contrast between the particles, which is beneficial for the optical tracking algorithms, two colour particle mixture were used (shown in Figure 13).



Figure 13: Multicolour particle mixture SB 30/50.

Tube configurations

To maximize the contact and thus potential heat transfer between the particles and the tubes, the staggered type tube configuration was chosen. The basic tube configuration layout is shown in Figure 14, where 3 main parameters were varied. These parameters are the outer tube diameter D, the horizontal gap between the tubes, which was considered as a function of the biggest particle diameter Dp and the diagonal pitch, which is considered as a function of the outer tube diameter. The used configurations and their parameters are listed in Table 6.

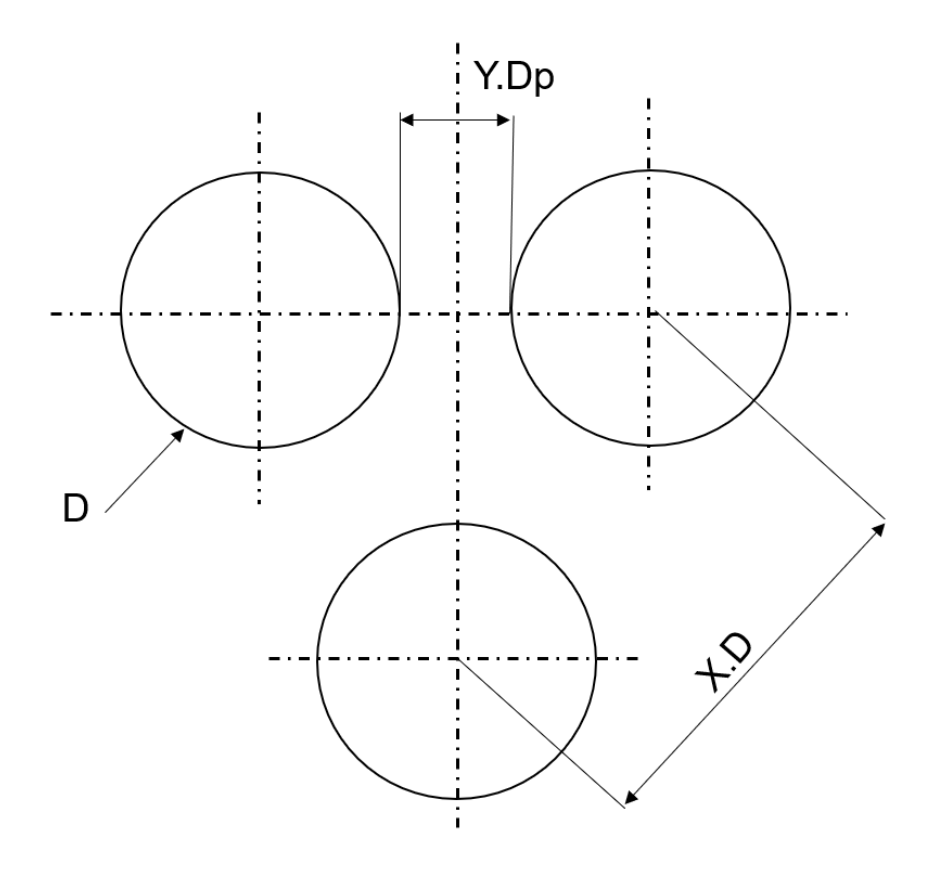


Figure 14: Tube configuration layout.

Table 6: Overview of the tube configuration parameters.

Config	X	Υ	D_tube (mm)	Horizontal pitch (mm)	Vertical pitch (mm)	Gap between tubes (mm)	Number of tubes in row
1	1.15	15	60.3	69.6	59.9	9	4
2	2	10	60.3	66.3	116.0	6	4
3	2	10	21.3	27.3	40.4	6	9.5
4	2	5	21.3	24.3	40.8	3	9.5
5	2	10	33.7	39.7	64.4	6	6.5
6	2	5	33.7	36.7	64.9	3	6.5
7	1.5	10	33.7	39.7	46.5	6	6.5
8	1.1	10	33.7	39.7	31.3	6	6.5
9	4	10	13.6	20.2	53.9	6	12
10	3.5	10	21.3	28	73.3	6	9.5
11	3	10	21.3	28	62.3	6	9.5
12	2.5	10	21.3	28	51.4	6	9.5
13	4	10	21.3	28	84	6	9.5

Results

Transportation system characteristics and energy requirements

The particles mass-flow characteristics were considered as a function of the screw conveyor revolutions. The double helix screw with outer diameter of 46mm and total length of 270mm (shown in Figure 15) was spun with 300 W electromotor with gearbox at constant rate for a fixed time, while the particles were fed from the end of the conveyor line into the separate vessel to be weighted. A particle mass-flow characteristics were obtained for multiple spinning regimes, which is shown in Figure 16. The particle mass-flow can be effectively regulated in range of 66 – 165 g/s. Note that the trend is not entirely linear, which is probably caused by losses induced in the ejector, where particles and air are mixing.

Furthermore, the pressure losses were measured between two points laying on the vertical conveyor line with inner diameter of 28mm. The pressure loss is linearly scaling as the particle to air mass-flow ratio is increasing. This relation is shown in Figure 17, where pressure loss per 1m of the conveying line is considered. This relation comes handy for the energy requirements estimation when scaling up the conveying line.

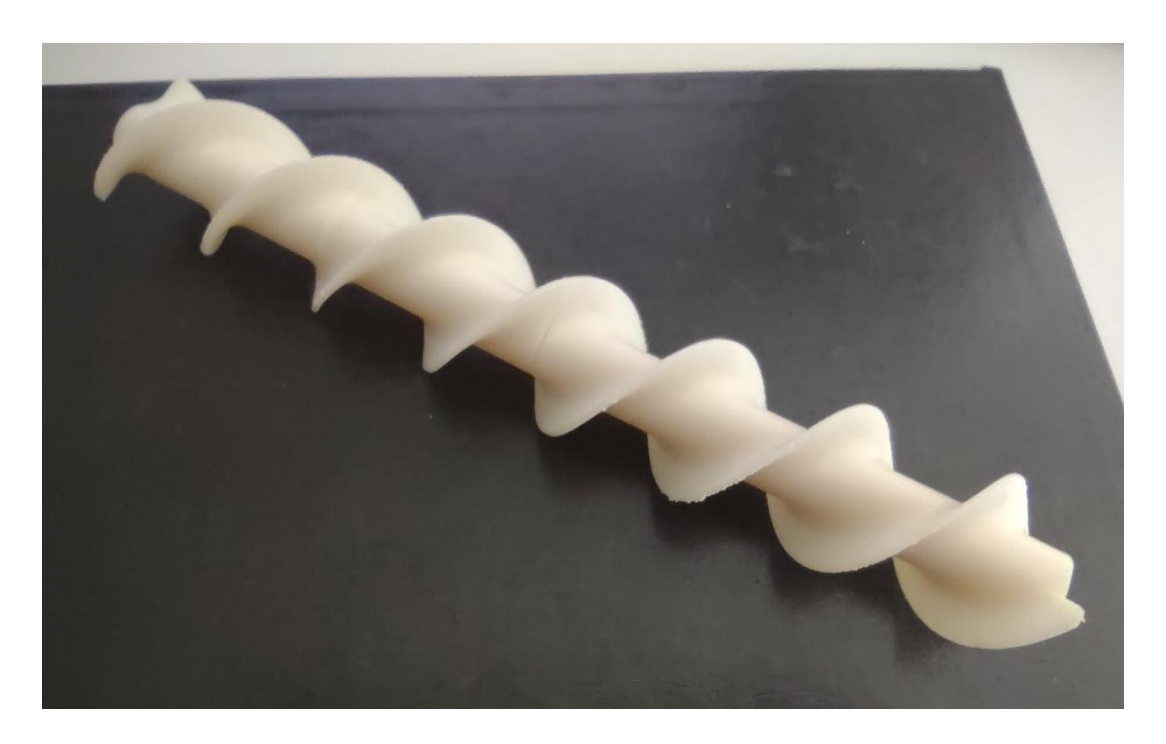


Figure 15: Screw for conveying the particles.

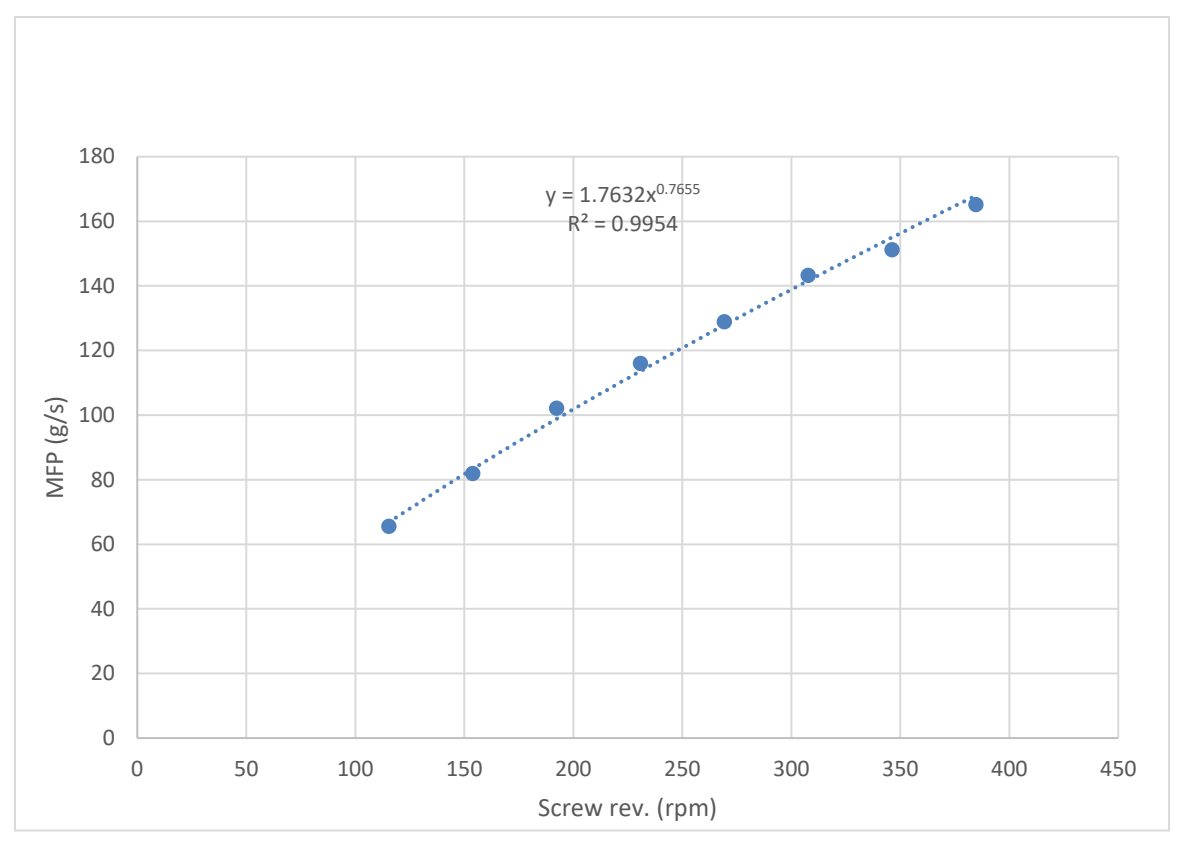


Figure 16: Particles mass-flow characteristics of the screw conveyor.

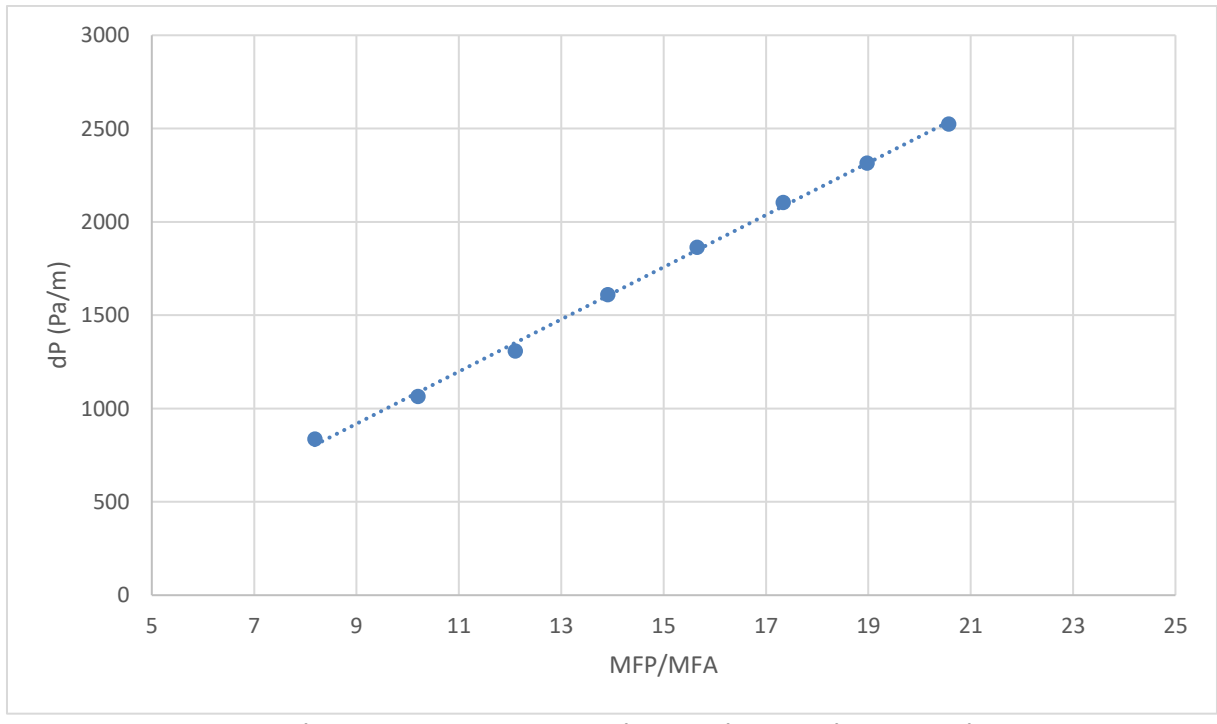


Figure 17: Pressure loss per 1m in vertical pipe during the particle transportation.

Particle velocity fields between the tube banks

To evaluate the particle flow between the tube banks, the air flow was fixed at 25m³/h and the particle mass-flow was varied and video recorded for each configuration. The records were then postprocessed with particle image velocimetry (PIV) algorithm and the velocity fields were obtained.

The resulting examples of the velocity fields between the tube banks are present in Figure 18, Figure 19 and Figure 20. where on the first glance is visible that the vertical spacing of the tubes affects the height of the stagnation zone above each tube. The tighter spacing, the smaller the stagnation zone is. While comparing Figure 19 and Figure 20, where the only difference is the particles mass-flow, it can be seen that the height of the stagnation zone is relatively unchanged. Thus, it can be stated, that the particles mass-flow does not affect the flow pattern around the tubes and depends mainly on the geometry, namely the vertical pitch of the tubes. A second smaller stagnation zone is also present on the downstream of the tube. To quantify the results, an angle section and height of both stagnation zones were measured in CAD software as it is shown in Figure 21. All the measured data are listed in Table 7.

The measured data confirms that the size of the top stagnation zone is depended on the vertical pitch. Interesting shift in height of the top stagnation zone can be noted on the data plotted in Figure 22. where the top stagnation zone height grows linearly up to the point where the ratio of vertical pitch to tube diameter is about 1.9. Then the top stagnation zone starts to collapse until the point, where further increase in vertical pitch does not have any effect and the top stagnation zone remains constant. It follows that the neighbouring tube rows does not affect the particle flow anymore, when the vertical pitch to tube diameter ratio is above 4.

The height of the bottom stagnation zone, that is always present, seem unchanged and can be expressed by linear expression as a function of the tube diameter shown in Figure 23.

The effect of variation in the horizontal pitch, where the gaps of $5xD_p$ and $10xD_p$ were tested, was not noticeable in relation to the flow pattern around the tube, however the flow with tighter gap wasn't always consistent, hence gap of $10xD_p$ would be preferred.

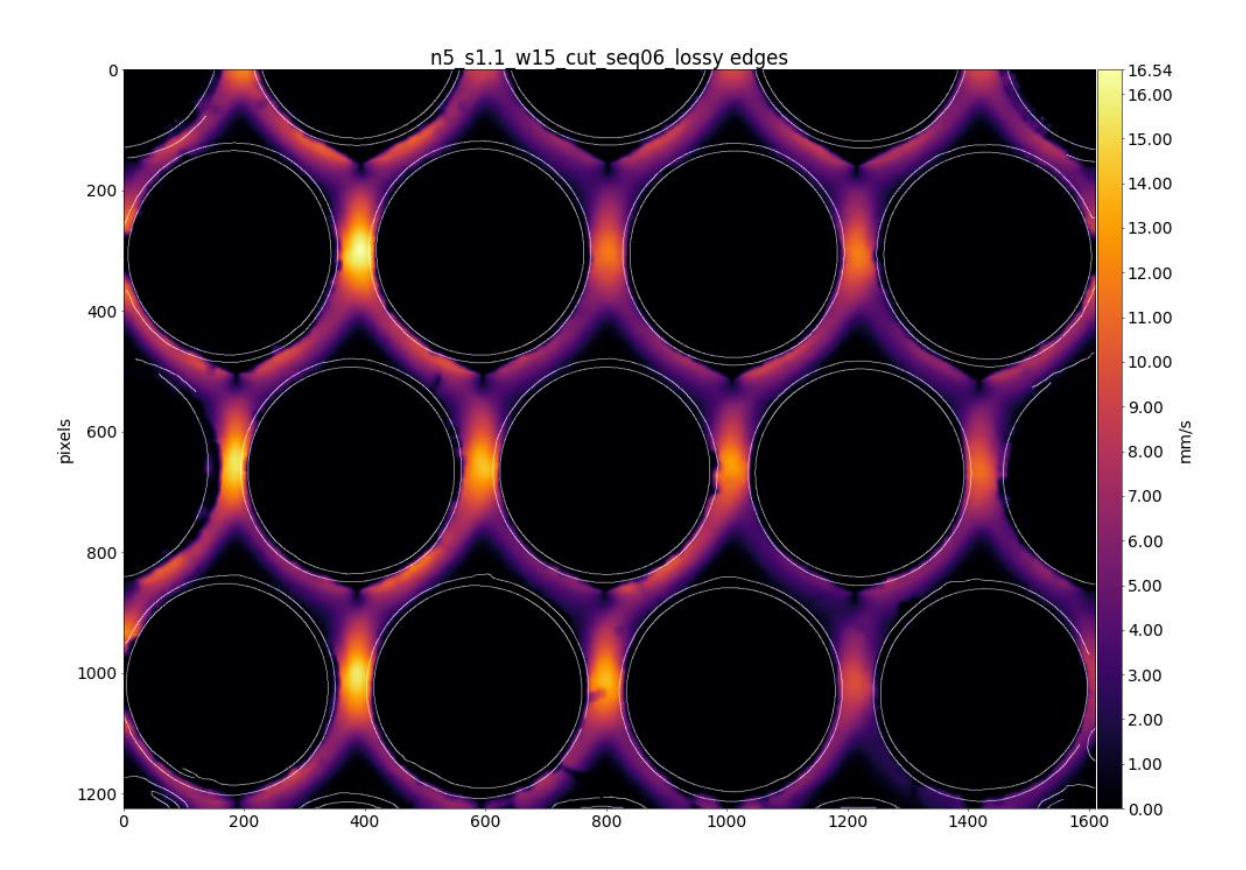


Figure 18: Configuration 1 - velocity field - MPF = 168g/s.

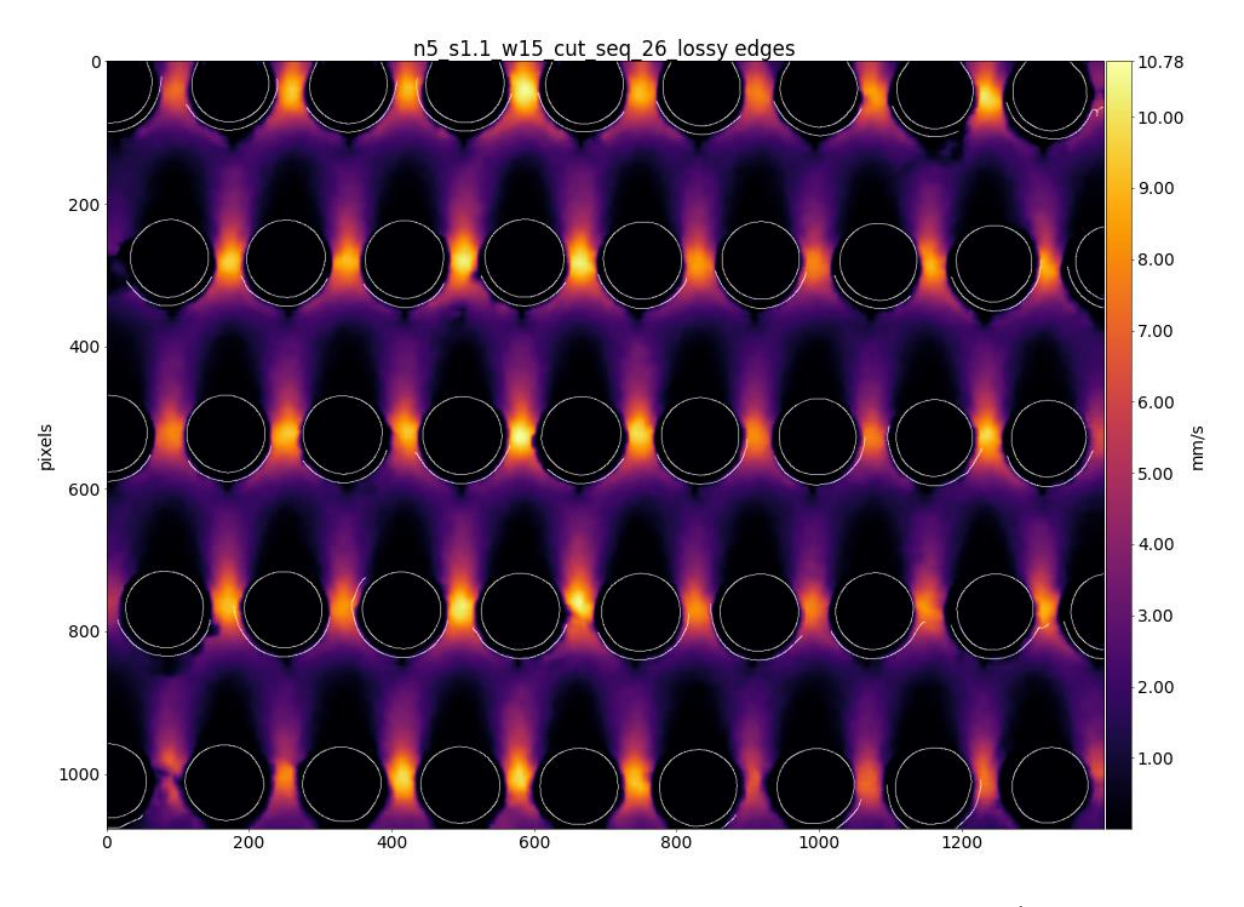


Figure 19: Configuration 3 - velocity field - MPF = 168g/s.

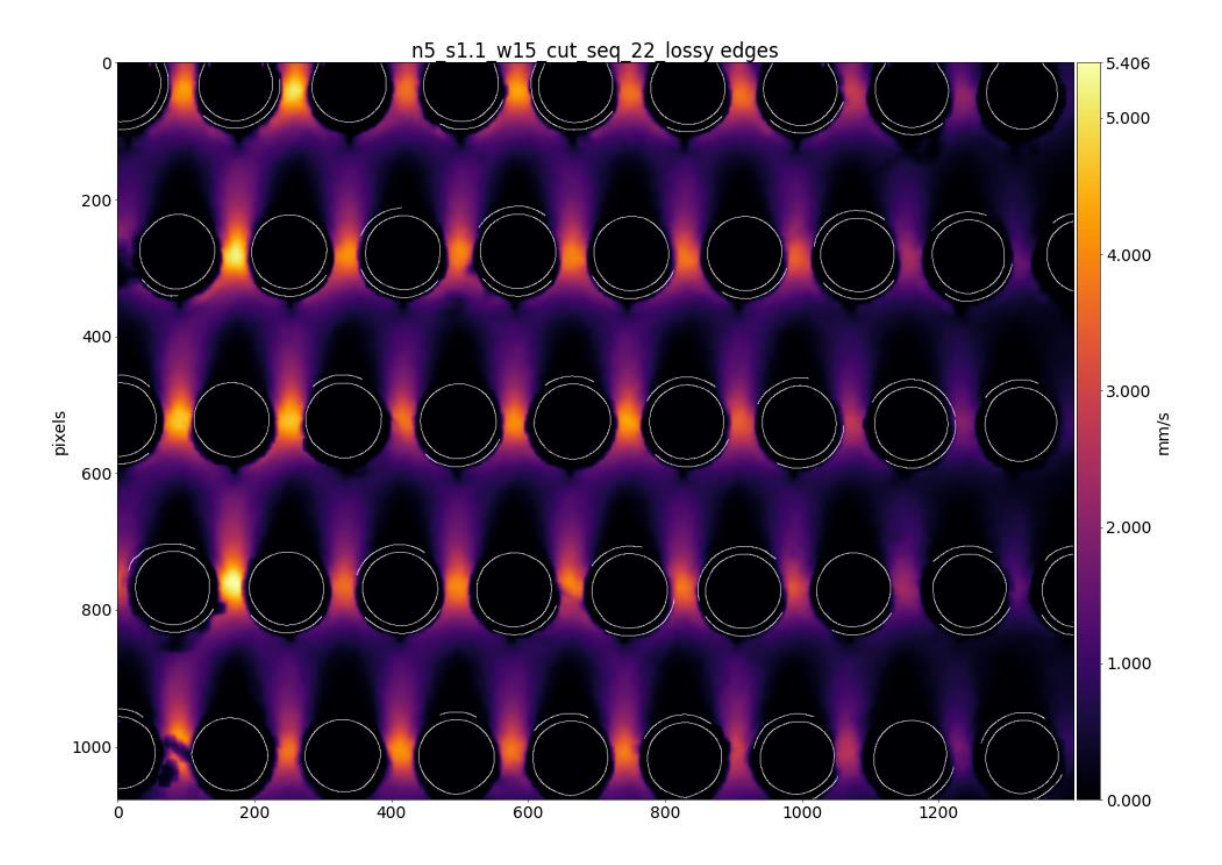


Figure 20: Configuration 3 - velocity field - MPF = 67g/s.

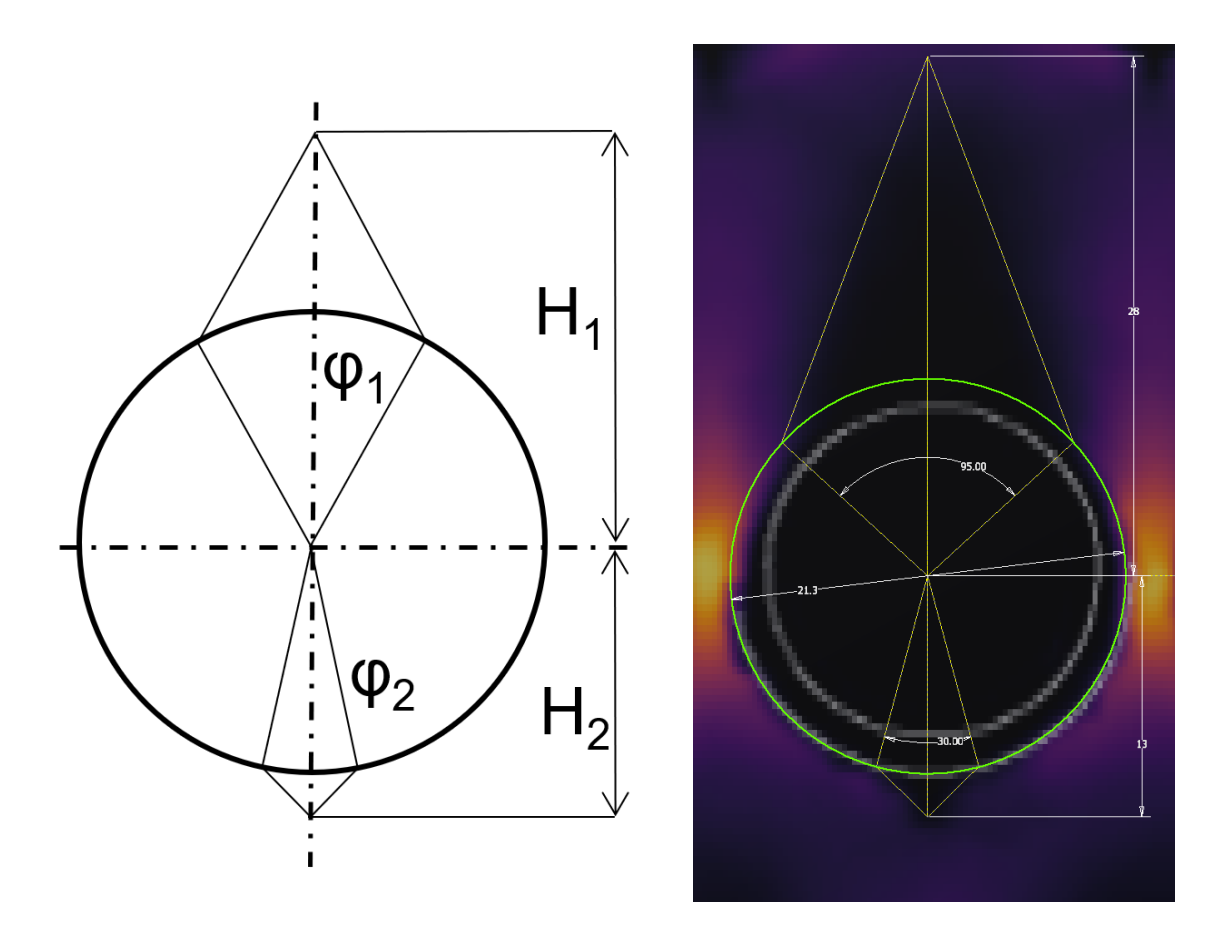


Figure 21: Measuring the height and angle section of the stagnation zones.

Table 7: Measured data from the particle velocity fields.

Configuration	MFP (kg/s)	ф1 (°)	ф2 (°)	H1 from axis (mm)	H2 from axis (mm)
	49	50	30	40	34
	49	50	30	40	34
-	83	50	30	40	34
1	114	50	30	40	34
-	142	50	30	40	34
-	168	50	30	40	34
	67	95	30	75	34
	83	95	30	75	34
2	114	95	30	75	34
_	142	95	30	75	34
	168	95	30	75	34
	67	95	30	28	13
	83	95	30	28	13
3	114	95	30	28	13
_	142	95	30	28	13
	168	95	30	28	13
	67	95	30	28	13
	83	95	30	28	13
4	114	95	30	28	13
-	142	95	30	28	13
	168	95	30	28	13
	67	95	30	40	20
	83	95	30	40	20
5	114	95	30	40	20
	142	95	30	40	20
	168	95	30	40	20
	67	95	30	40	20
	83	95	30	40	20
6	114	95	30	40	20
	142	95	30	40	20
	168	95	30	40	20
	83	95	30	34	20
7	114	95	30	34	20
7	142	95	30	34	20
	168	95	30	34	20
	83	36	30	22	20
8	114	36	30	22	20
O	142	36	30	22	20
	168	36	30	22	20
9	83	95	45	11	9.5
<i>9</i>	142	95	45	11	9.5
10	83	95	30	17	13
	142	95	30	17	13

COMPASsCO2 - Components' and Materials' Performance for Advanced Solar Supercritical CO2 Power Plants

11	83	95	30	18	13
	142	95	30	18	13
12	83	95	30	19.5	13
	142	95	30	19.5	13
13	83	95	30	17	13
	142	95	30	17	13

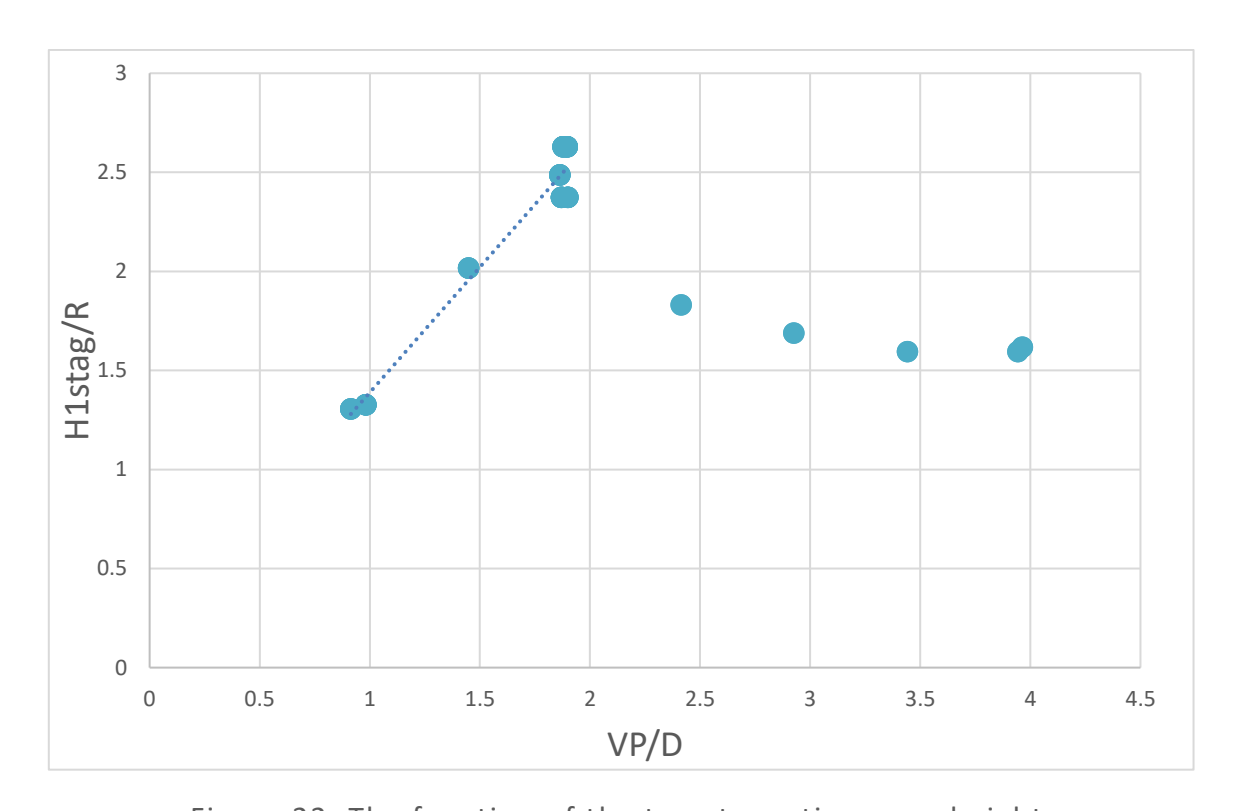


Figure 22: The function of the top stagnation zone height.

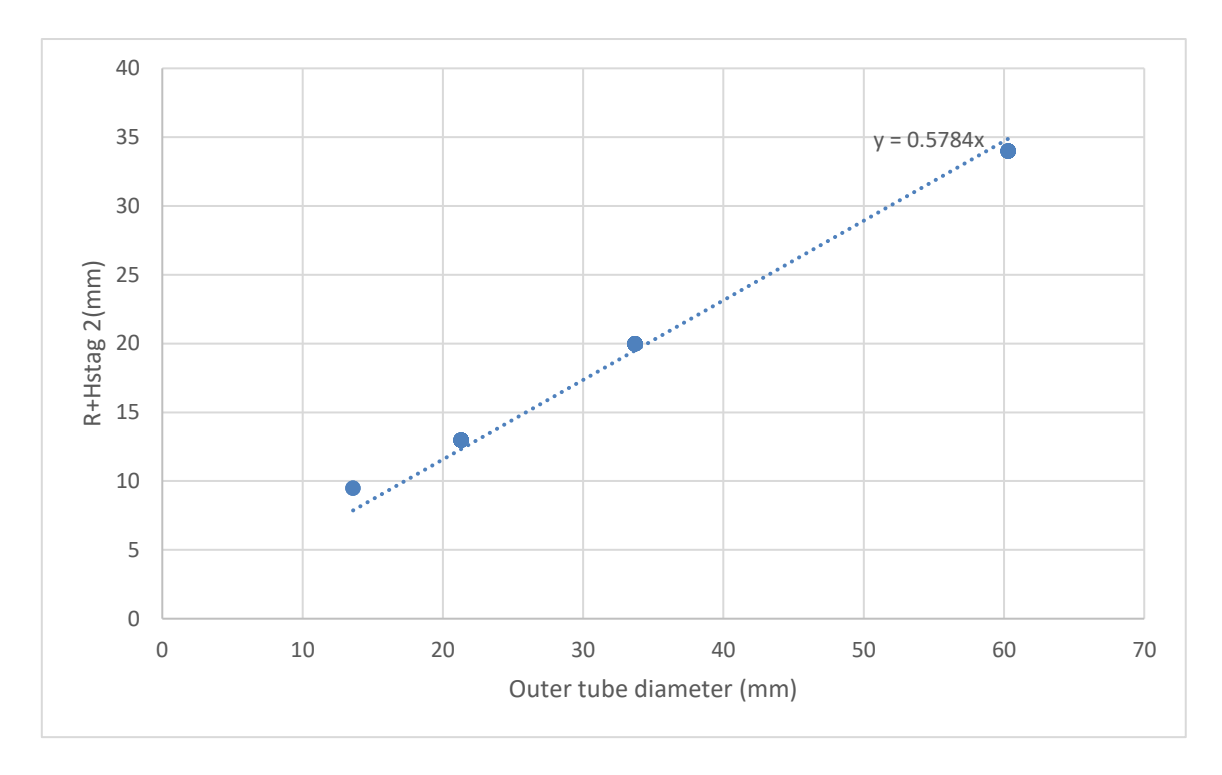


Figure 23:The function of the bottom stagnation zone height.

Horizontal angle displacement sensitivity

During the tests, some inconstancy within the flow in the radial direction was noticeable, when the experimental rig was not perfectly horizontally aligned as it is shown in Figure 24. This effect was further examined for different angle displacement as it is present in Figure 25, where the particle flow become stagnant near the side wall. This stagnation trend advances in the radial direction as the inclination gets bigger. The inclination of only 1.5° had tremendous effect on the flow distribution in radial direction as it is shown in Figure 25. This is probably caused by the fact that the particles can carry the shear stresses caused by the interactions with the walls that further propagates into the flow. Hence it is very important to ensure this horizontal alignment in the following builds and experiments.

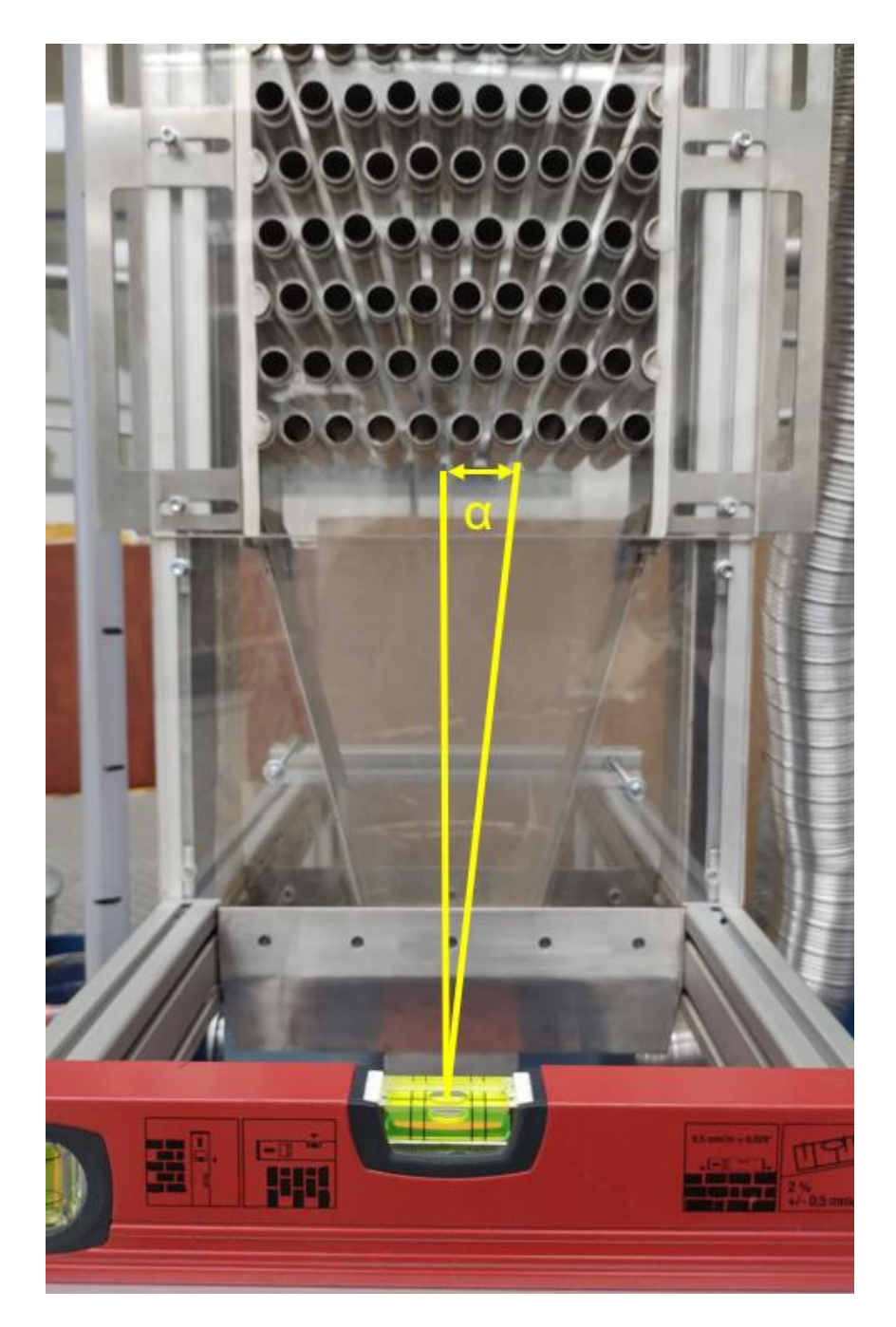
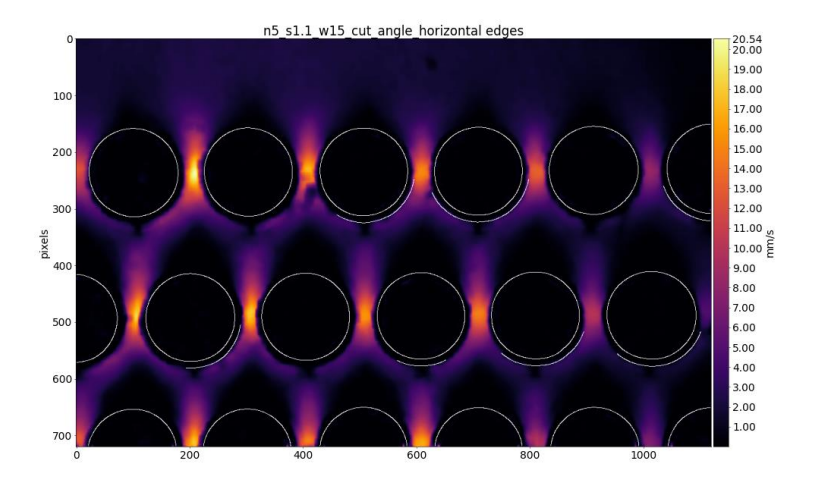
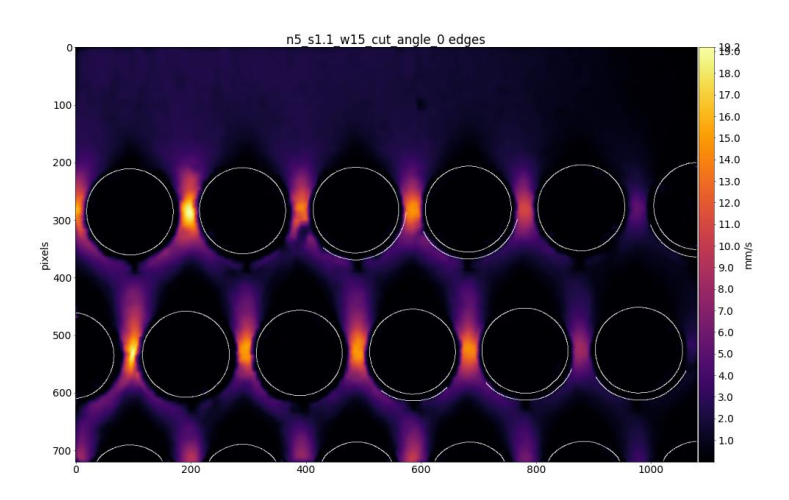


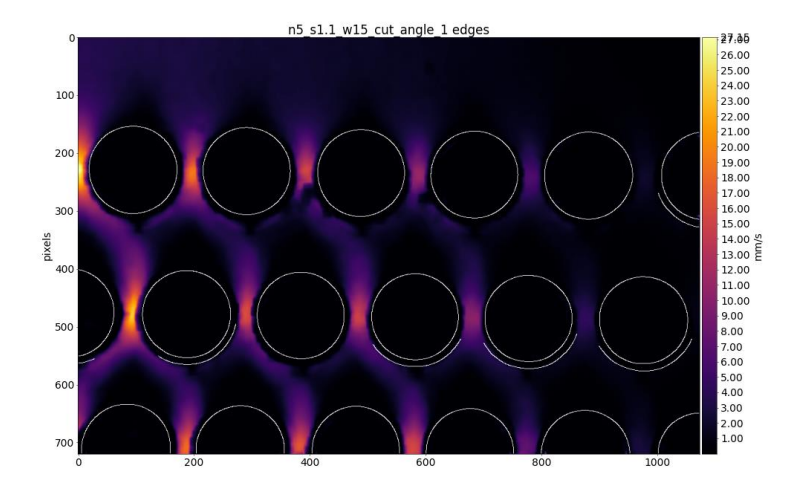
Figure 24: Angle displacement scheme.



 $\alpha = 0^{\circ}$



 $\alpha = 0.5^{\circ}$



 $\alpha = 1.5^{\circ}$

Figure 25: Angle displacement sensitivity - radial distribution

Heat transfer modelling

As the shape and size of the stagnation zones will play a significant role in heat transfer, a simple 1D model considering that effect is presented. A single tube 19.05x2.5mm is considered in the model with the stagnation zones, modelled based on the data obtained from the cold test. The proposed model considers an differential of the total heat transfer resistance as a function of the angle and can be defined as:

$$dR_{tot(d\varphi)} = dR_{ID(\varphi)} + dR_{COND(d\varphi)} + dR_{stag(d\varphi)} + dR_{OD(d\varphi)}$$

Where R_{ID} is the heat resistance due to the convection on the inner diameter and is defined as:

$$dR_{ID(d\varphi)} = \frac{1}{h_{ID}r_{ID}d\varphi}$$

Where h_{ID} is the convective heat transfer coefficient. The R_{COND} is the heat resistance due to the heat conduction within the tube thickness, defined as:

$$dR_{COND(d\varphi)} = \frac{r_{ID}}{\lambda_{tube} r_{tube_ave} d\varphi} \ln \left(\frac{r_{OD}}{r_{ID}}\right)$$

Where λ_{tube} is the thermal conductivity of the tube material. The *Rstag* is the heat resistance due to the presence of the stagnation zone and it is defined as:

$$dR_{stag(d\varphi)} = \frac{r_{OD}}{\lambda_{eff}r_{stag\ ave}d\varphi} \ln\left(\frac{r_{OD}}{r_{ID}}\right)$$

Where λ_{eff} is the effective conductivity of the stagnation zone, defined as:

$$\lambda_{eff} = \lambda_{Air} \varepsilon + (1 - \varepsilon) \lambda_{particles}$$

Where ε is the porosity. In case of the stagnation zone on the downstream of the pipe, it is considered that consist only from the air, hence the effective conductivity there would be equal to the conductivity of air. Finally the R_{OD} is the thermal resistance due to the convection on the outer boundary and is defined as:

$$dR_{OD(d\varphi)} = \frac{1}{h_{OD}r_{OD}d\varphi}$$

Then the average total heat transfer resistance can be defined as:

$$R_{tot} = \frac{\sum_{i=1}^{n} dR_{tot(i)}}{n} \left[\frac{m \cdot K}{W} \right]$$

Example case is presented, considering the material properties and variables listed in Table 8. The resulting geometry is projected to the polar coordinates with its boundaries ant it is shown in Figure 26. Then the individual heat resistances can be calculated and are plotted in Figure 27. There it can be seen that the highest heat transfer resistance is located on the bottom section of the tube, due to the air gap within

the bottom stagnation zone. The heat transfer resistance contribution in this section would remain unchanged no matter to the tube configuration or the flow regime. However the influence of the heat transfer resistance on the top section can be influenced by changing the tubes vertical pitch.

The same procedure was done for several data points with different vertical pitch to tube diameter ratios. The comparison of the total heat transfer resistances is present in Figure 28, where it is visible the lowest heat transfer resistance on the top section for the VP/D = 1, then the heat resistance reaches maximum at about VP/D = 2, and then it decreases again for VP/D = 3.5. The comparison of the average heat transfer resistances is shown in Table 9, where for reference is considered a case that is unaffected by the stagnation zones. From the comparison is visible that the stagnation zones significantly affect the average heat transfer resistance, with the maximum difference up to 24 % compared to the reference case. It is also noteworthy the difference between the VP/D = 2 and VP/D = 1 where the difference is almost 9 %, which is quite significant change, considering only the geometrical placement of the tubes.

Table 8: List of considered variables.

D (mm)	19.05		
tube thickness (mm)	2.5		
VP/D	1.5		
h _{ID} (W/m2/K)	3837		
h _{OD} (W/m2/K)	180		
$\lambda_{Air}(W/m/K)$	0.066		
λ _{paricles} (W/m/K)	0.5		
λ _{tube} (W/m/K)	15		
€ (-)	0.443		

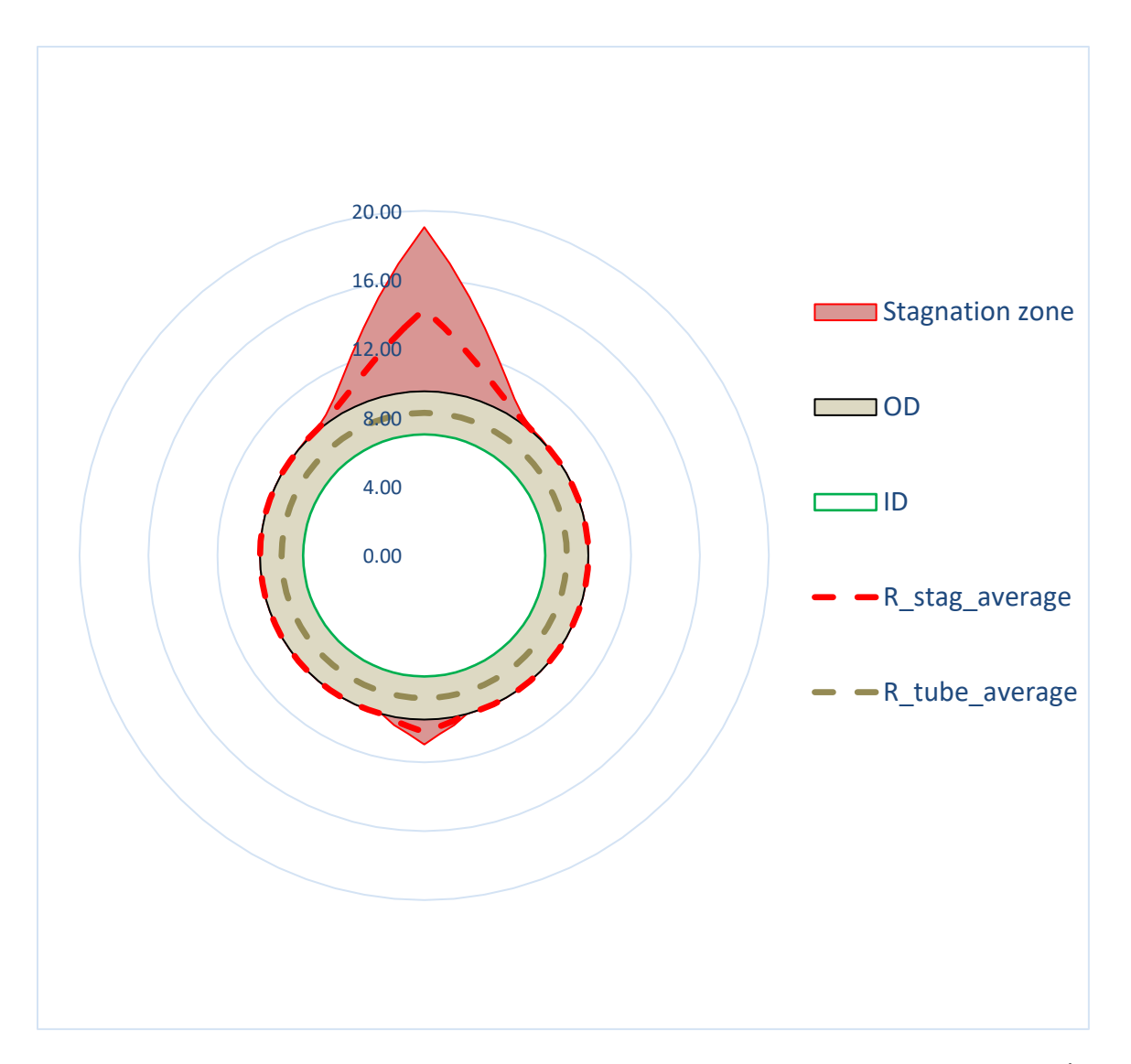


Figure 26: Model of the stagnation zones around a single tube D=19.05; VP/D=1.5.

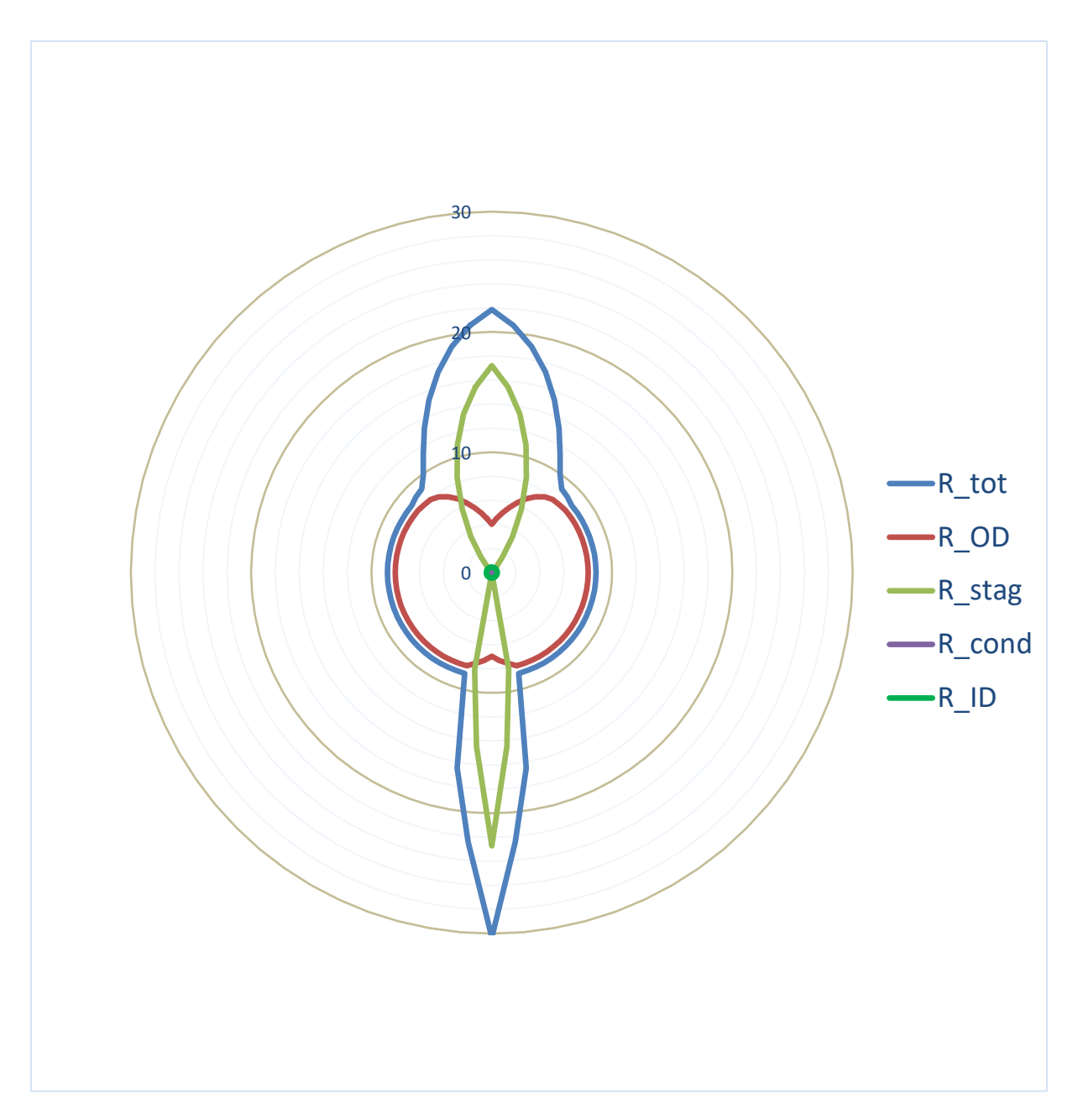


Figure 27: Plotted individual heat transfer resistances for a single tube D=19.05; VP/D = 1.5.

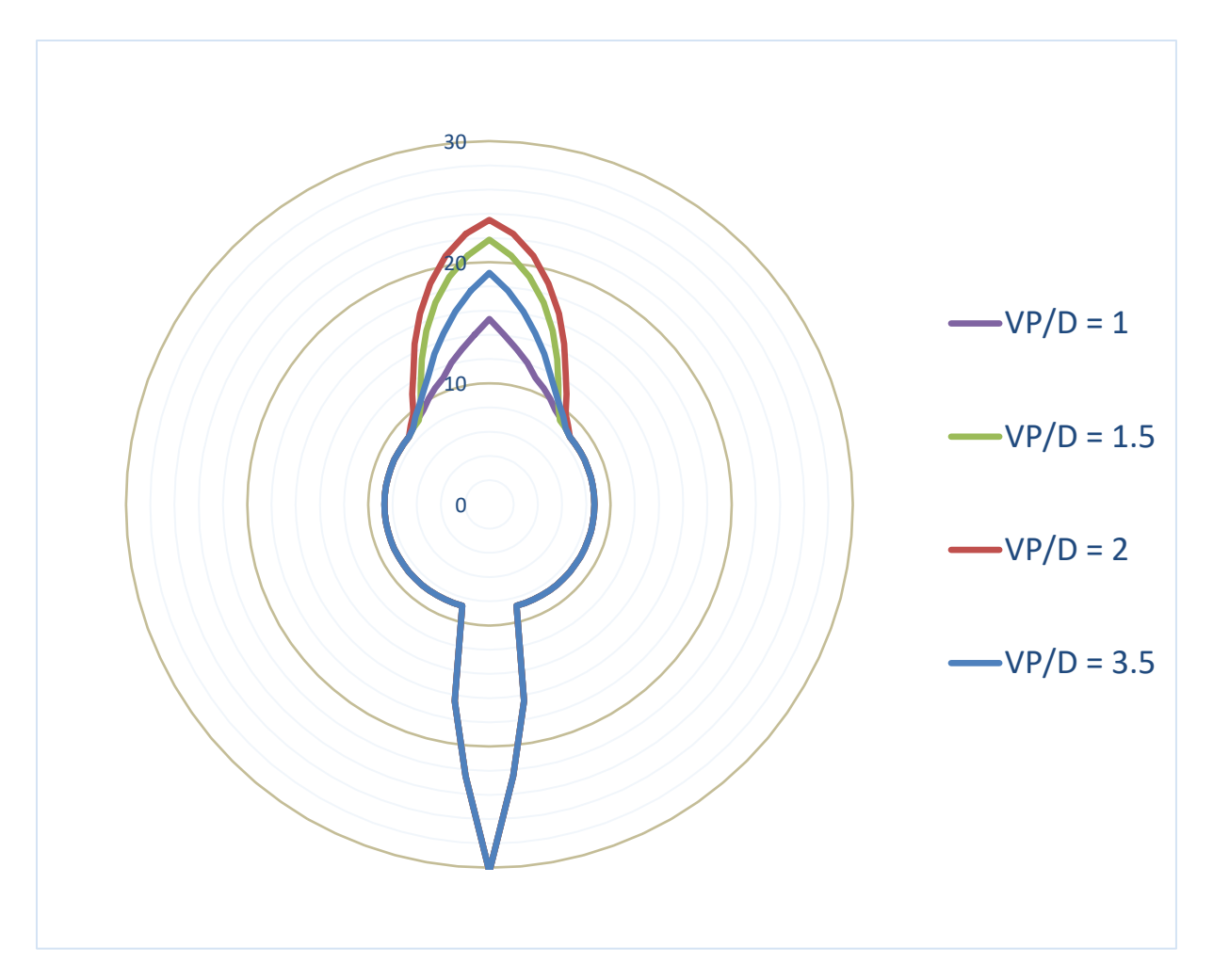


Figure 28: Comparison of the total heat transfer resistance for various VP/D ratios.

Table 9: Comparison of average heat transfer resistances for different vertical tube spacing.

VP/D	R_tot ave (mK/W)	1/R (W/m/K)	Increase (%)
Ref.	0.12	8.31	-
1	0.14	7.04	15.3
1.5	0.15	6.52	21.6
2	0.16	6.32	23.9
3.5	0.15	6.74	18.9

Conclusion

The knowledge and the benefits of the experiments made with the cold particles flow can be summed in the following bullet points:

- The concept of the particle transportation system was successfully tested and validated, and it can be further implemented into the next stages of the project.
- The particle flow pattern and its distribution around the tubes mainly depends on the tubes vertical spacing.
- A small inclination in the horizontal plane causes inconsistent flow distribution in radial direction.
- The tubes vertical spacing has a significant influence on the heat transfer, where the tube spacing with ratio of VP/D = 2 would have the worst performance, since the top stagnation zone is the highest. Hence interval of VP/D <1.75; 3> should be avoided, due to its increased heat transfer resistance.
- A good trade-off for the vertical pitch seems to be VP/D > 3.5, since the thermal resistance slightly decreases and it is also favourable for the manufacturing purposes (higher bending radius = better).